

Li Lijuan (Orcid ID: 0000-0001-8814-5738)
Yu Yongqiang, yong (Orcid ID: 0000-0001-8596-3583)
Lin Pengfei (Orcid ID: 0000-0003-2361-0066)
Xie Jinbo (Orcid ID: 0000-0002-3003-9155)
Zhou Tianjun (Orcid ID: 0000-0002-5829-7279)
Liu Li (Orcid ID: 0000-0001-7643-3732)
Xie Zhenghui (Orcid ID: 0000-0002-3137-561X)
Zhang Lixia (Orcid ID: 0000-0002-8424-3741)
Liu Hailong (Orcid ID: 0000-0002-8780-0398)
Jia Binghao (Orcid ID: 0000-0002-9354-0457)
Wang Bin (Orcid ID: 0000-0002-3133-7197)

The Flexible Global Ocean–Atmosphere–Land System Model Grid-Point Version 3 (FGOALS-g3): Description and Evaluation

Lijuan Li¹, Yongqiang Yu^{1,5,6}, Yanli Tang¹, Pengfei Lin^{1,5}, Jinbo Xie¹, Mirong Song¹, Li Dong^{1,5}, Tianjun Zhou^{1,5}, Li Liu², Lu Wang^{3,1}, Ye Pu¹, Xiaolong Chen¹, Lin Chen^{3,1}, Zhenghui Xie^{1,5}, Hongbo Liu¹, Lixia Zhang¹, Xin Huang¹, Tao Feng^{4,1}, Weipeng Zheng^{1,5}, Kun Xia¹, Hailong Liu^{1,5,6}, Jiping Liu¹, Yan Wang¹, Longhuan Wang¹, Binghao Jia¹, Feng Xie^{1,7}, Bin Wang^{1,5}, Shuwen Zhao^{1,5}, Zipeng Yu¹, Bowen Zhao¹, Jilin Wei¹

¹State Key Laboratory of Numerical Modeling for Atmospheric Sciences and Geophysical Fluid Dynamics (LASG), Institute of Atmospheric Physics, Chinese Academy of Sciences, Beijing, China

²Center of Earth System Science (CESS), Tsinghua University, Beijing, China

³Key Laboratory of Meteorological Disaster, Ministry of Education (KLME)/Joint International Research Laboratory of Climate and Environmental Change (ILCEC)/Collaborative Innovation Center on Forecast and Evaluation of Meteorological Disasters (CIC-FEMD), Nanjing University of Information Science and Technology, Nanjing, China

⁴Department of Atmospheric Sciences, Yunnan University, Kunming, China

⁵College of Earth and Planetary Sciences, University of Chinese Academy of Sciences, Beijing, China

⁶Center for ocean Mega-Science, Chinese Academy of Sciences, Qingdao, China

This article has been accepted for publication and undergone full peer review but has not been through the copyediting, typesetting, pagination and proofreading process which may lead to differences between this version and the Version of Record. Please cite this article as doi: 10.1029/2019MS002012

⁷Anhui Meteorological Observatory, Hefei, China

Corresponding author: Bin Wang (wab@lasg.iap.ac.cn)

Key Points:

- This paper describes FGOALS-g3 and its experiment design for CMIP6
- Historical, Pre-industrial and Scenario simulations are evaluated
- Climate drift is small in Pre-industrial simulation and mean climate and climate variabilities at different temporal scales are realistic in historical runs

Abstract

This paper introduces the Flexible Global Ocean–Atmosphere–Land System Model: Grid-Point Version 3 (FGOALS-g3) and evaluates its basic performance based on some of its participation in the sixth phase of the Coupled Model Intercomparison Project (CMIP6) experiments. Our results show that many significant improvements have been achieved by FGOALS-g3 in terms of climatological mean states, variabilities, and long-term trends. For example, FGOALS-g3 has a small ($-0.015^{\circ}\text{C}/100\text{ yr}$) climate drift in 700-yr pre-industrial control (piControl) runs, and smaller biases in climatological mean variables, such as the land/sea surface temperatures (SST), seasonal soil moisture cycle, compared with its previous version FGOALS-g2 during the historical period. The characteristics of climate variabilities, e.g., MJO eastward/westward propagation ratios, spatial patterns of interannual variability of tropical SST anomalies, and relationship between the East Asian Summer Monsoon and El Niño-Southern Oscillation (ENSO), are well captured by FGOALS-g3. In particular, the cooling trend of globally averaged surface temperature during 1940–1970, which is a challenge for most CMIP3 and CMIP5 models, is well reproduced by FGOALS-g3 in historical runs. In addition to the external forcing factors recommended by CMIP6, anthropogenic groundwater forcing from 1965 to 2014 was incorporated into the FGOALS-g3 historical runs.

Plain Language Summary

The sixth phase of the Coupled Model Intercomparison Project (CMIP6) is a crucial support for the sixth Assessment Report of Intergovernmental Panel on Climate Change (IPCC AR6), and will also provide important foundation for research in climate change in the next few years. This paper gives the description of FGOALS-g3 model, its experiment configurations and the experiments conducted according to the experimental design of CMIP6, and evaluates the preliminary performance of model simulation. This work offers references to CMIP6 data users and provides enormous output datasets for assessing and understanding climate change.

Introduction

State-of-the-art climate system models have been widely applied in the climate sciences across multiple scales in time and space, for example, they are the tool available to predict or project future climate change (IPCC, 2013). They are established on the mathematical formulations of the natural laws that govern the evolution and interaction of the five components of the climate system (i.e., the atmosphere, ocean, cryosphere, land, and biosphere). Associated with rapid progress in observations, dynamic theories, and computer performance, continuous advances have been made in developing component and fully coupled models during the past few decades.

Since the late 1980s, considerable efforts have been made in developing, assessing, and improving atmospheric, oceanic, land, and sea ice models, and coupled climate models, at the State Key Laboratory of Numerical Modeling for Atmospheric Sciences and Geophysical Fluid Dynamics (LASG), Institute of Atmospheric Physics (IAP), Chinese Academy of Sciences (CAS). To-date, there have been six generations of coupled climate models (Zhang et al., 1992; Chen et al., 1997; Wu et al., 1998; Yu et al., 1998, 2002, 2004; Li et al., 2013a; Bao et al., 2013) developed at LASG-IAP. These coupled models have also contributed to each phase of the Coupled Model Intercomparison Project (CMIP) (Covey et al., 2003; Meehl et al., 2005) and assessment reports of Working Group I of the Intergovernmental Panel on Climate Change (IPCC) (IPCC, 1992, 1995, 2001, 2007, 2013).

The latest generation of climate system models developed at LASG-IAP is Version 3 of the Flexible Global Ocean–Atmosphere–Land System model (FGOALS3), which includes three parallel subversions (FGOALS-g3, FGOALS-f3-L, and FGOALS-f3-H). All three subversions were established based on a similar coupling framework, in which atmospheric, oceanic, sea ice, and land component models are connected via a common flux coupler. The same oceanic and sea ice models are shared by these three subversions, but different atmospheric and land component models are used. The present study describes the basic configuration of the coupled model FGOALS-g3 and evaluates its performance in terms of climatological means, climatic variability, and long-term climate trend. The four component models of FGOALS-g3 include Version 3 of the Grid-Point Atmospheric Model of LASG-IAP (GAMIL3) for the atmosphere, Version 3 of the LASG-IAP Climate System Ocean Model (LICOM3) for the ocean, Version 4 of the Los Alamos sea ice model for sea ice (<http://climate.lanl.gov/Models/CICE>), and the CAS-Land Surface Model (CAS-LSM) for the land (Xie et al., 2018). According to the numerical experiment design for CMIP6 (Eyring et al., 2016), we have conducted lots of CMIP6 experiments, including the Diagnostic, Evaluation, and Characterization of Klima (DECK), historical simulations, Scenario Model Intercomparison Project (ScenarioMIP), Global Monsoons Model Intercomparison Project (GMMIP), and Ocean Model Intercomparison Project (OMIP), which are also published online in the Earth System Grid Federation (ESGF). And we are also conducting other MIPs, such as the Paleoclimate Modeling Intercomparison Project (PMIP) and Decadal Climate Prediction Project (DCPP). In the present study, DECK, historical, and ScenarioMIP

simulations are analyzed and evaluated with emphasis on the mean state, and climate variability and change.

The remainder of this paper is organized as follows. Section 2 documents the major developments in FGOALS-g3 components and experiment design, and describes the stability of the coupled system after the spin-up processes. Section 3 shows results from climate mean states to major climate variability modes. The model performance for 20th century climate and Asian Monsoon simulations are also assessed in Section 3. Finally, section 4 provides a summary and discussion.

1. Model description and experimental design

2.1 Model description

GAMIL3 is updated from GAMIL2 (Li et al., 2013b). Both versions use the same finite difference dynamical core, which conserves many properties, such as total mass and effective energy under the standard stratification approximation (Wang et al., 2004), and employ a 26 vertical σ -layers (pressure normalized by surface pressure) coordinate with the model top at 2.194 hPa. Compared with GAMIL2, GAMIL3 has many modifications with respect to parallel computing, horizontal resolution, water vapor advection scheme, physical processes, and external forcings. GAMIL3 utilizes a two-dimensional hybrid parallel decomposition (Liu et al., 2014) replacing the one-dimensional parallel decomposition in the meridional direction, increases the horizontal resolution from $\sim 2.8^\circ$ (128×60) to $\sim 2^\circ$ (180×80), and improves water vapor conservation through modification of the two-step shape-preserving advection scheme (TSPAS, Yu, 1994). With regards to physical processes, GAMIL3 incorporates a convective momentum transport scheme (Wu et al., 2007); adopts a simple stability-based stratocumulus cloud fraction scheme based on estimated inversion strength (EIS; Guo & Zhou, 2014); and involves a simple parameterization of the second version of the Max Planck Institute Aerosol Climatology model (MACv2-SP) for anthropogenic aerosol effects (Stevens et al., 2017; Shi et al., 2019) and an improved boundary layer scheme that includes entrainment at the top of the boundary layer, longwave radiative cooling at the top of stratocumulus clouds, and turbulent kinetic energy (TKE) (Sun et al., 2016). In addition, the external forcings recommended by CMIP6 were updated and their impacts on model stability, 20th century global warming, and ENSO were evaluated by FGOALS-g2 (Nie et al., 2019).

CAS-LSM is the land component of FGOALS-g3 with the same horizontal resolution as the atmospheric component, and is based on the Community Land Model Version 4.5 (CLM4.5). However, it includes unique improvements and additions to the land processes with respect to CLM4.5, such as groundwater lateral flow (Xie et al., 2012; Zeng et al., 2016a, 2016b, 2018), anthropogenic groundwater exploitation (Zou et al., 2014, 2015; Zeng et al., 2016b, 2017), implementation of a new frozen soil parameterization including frost and thaw fronts (Gao et al., 2016, 2019), anthropogenic nitrogen discharge in rivers (Liu et al., 2019), and urban processes.

LICOM3 is updated from LICOM2 (Liu et al., 2012; Lin et al., 2016). Its dynamical core with a latitude–longitude grid structure is replaced by arbitrary orthogonal curvilinear

coordinates (Madec & Imbard, 1996; Murray, 1996; Yu et al., 2018). Preserved shape advection (Xiao, 2006) and the implicit vertical viscosity (Yu et al., 2018) are used. The St. Laurent et al. (2002) tidal mixing model (Yu et al., 2017) is introduced into LICOM3. In addition, the eddy-induced mixing of Redi (1982) and Gent and McWilliams (1990), and the buoyancy frequency (N^2) related thickness diffusivity of Ferreira et al. (2005), were added to the model. The chlorophyll-a dependent solar penetration of the Ohlmann (2003) scheme (Lin et al., 2007) and vertical mixing of Canuto et al. (2001, 2002) are used in LICOM3. A tripolar grid was chosen, with the North Pole split into two poles on-land, which can enlarge the time steps in the Arctic polar region and remove the spatial filter for momentum velocities and tracers. A B-grid was used for the horizontal distribution. The North Pole in the low-resolution LICOM3 is divided into two North Poles on-land at $65^\circ\text{N}/65^\circ\text{E}$ and $65^\circ\text{N}/115^\circ\text{W}$. The low-resolution LICOM3 has 360×218 horizontal grids. The vertical direction uses eta coordinates with 30 and 80 layers, but only the 30 layers were used for OMIP and CMIP6.

The sea ice model is the Los Alamos sea ice model Version 4.0, using the same grid as the oceanic model. This is an energy conserving thermodynamic model, which solves the dynamic and thermodynamic equations for five ice thickness categories, with one snow and four ice layers. For the dynamic component, the elastic–viscous–plastic rheology (Hunke & Dukowicz, 1997), mechanical redistribution scheme (Lipscomb et al., 2007), and incremental remapping advection scheme (Lipscomb & Hunke, 2004) are used. For the thermodynamic component, the Delta–Eddington radiative transfer scheme using inherent optical properties based on physical measurements (Briegleb & Light, 2007) is utilized.

There are two couplers: CPL7 developed at the National Center for Atmospheric Research (NCAR) and C-Coupler2 (Community Coupler Version 2) developed at Tsinghua University (Craig et al., 2012; Liu et al., 2018). Compared with CPL6 (Craig et al., 2005), CPL7 possesses improved memory and performance scaling that can support much higher resolution configurations. The computing performance of the coupled model using CPL7 was improved linearly by use of tens of thousands of CPUs. In addition, CPL7 has a more sophisticated computing resource control and a single executable, which allow the models to run flexibly and simplifies the machine requirements for the dispatcher. In addition to the Model Coupling Toolkit (MCT; Larson et al., 2005) that handles data transfer and interpolation for CPL7, C-Coupler2 was employed as a new option for these two functionalities, which provides exactly the same (bitwise identical) simulation results as MCT. Moreover, the coupling capability of FGOALS-g3 would be upgraded for future development with the new features of C-Coupler2 (i.e., dynamic 3-D coupling, flexible and automatic coupling generations, non-blocking data transfer, facilitation of increment coupling, and automatic remapping weight generation; Liu et al., 2018).

2.2 Experimental design

Prior to analyzing and evaluating the model performance, some basic experiments, including pre-industrial control (piControl), historical, and scenario runs were conducted according to the experimental design of CMIP6 (Eyring et al., 2016). In these experiments,

the coupling intervals of the atmospheric, land, and sea ice components are the same as the time-step (600 s) of GAMIL3, and the coupling frequency of LICOM3 is 8 times/day. Using this configuration, the piControl run spans 2000 yr, and acts as the baseline for other CMIP6-type simulations, where the first 700-yr (200–899) dataset after removing the first 200-yr spin-up was published on the ESG node. In all the piControl runs, the external forcing values were maintained at 1850 values.

Six member historical and four member scenario runs (shared socioeconomic pathways; SSPs) were performed using the time-varying external forcings recommended by CMIP6 (<https://esgf-node.llnl.gov/search/input4mips/>). The initial conditions are from years 370, 350, 330, 540, 465, and 700 of the piControl run for the six historical runs and from year 2015 of the first four historical runs for the four scenario runs. The forcings for the historical and scenario runs include monthly mean total solar irradiance (TSI) (Matthes, 2017), greenhouse gas (GHGs) concentrations with latitudinal changes and seasonality (Meinshausen et al., 2017), ozone concentrations, anthropogenic aerosol optical properties and an associated Twomey effect (Stevens, 2017), land use changes (Hurtt et al., 2017), and historical stratospheric aerosols. In addition, the anthropogenic groundwater exploitation forcing from 1965–2014 was adopted as an extra external forcing factor for the land component (Zeng et al., 2017).

The model tuning includes two steps: component model tuning with observed boundary condition and fully coupled model tuning. In the FGOALS-g3 tuning, the key targets include model stability (numerical stability and small drift), climate variability (mainly refers to ENSO) and mean state (small bias) of piControl runs through tuning the parameters (e.g., mixing parameter in LICOM3 and cloud-related parameters in GAMIL3) and the coupling intervals of LICOM3. In order to control the numerical instability possibly resulted from coupled processes, the LICOM3 time step is reduced from 3600s in uncoupled model to 2160s in the coupled model. Climate drift in the deep ocean is strongly associated with vertical mixing, thus the background vertical mixing coefficients depended on the latitude as suggested by Jochum (2009) are tuned, with the maximum $3.1 \times 10^{-5} \text{ m}^2 \text{ s}^{-2}$ around 30°S/N and minimum $0.3 \times 10^{-5} \text{ m}^2 \text{ s}^{-2}$ around the equator, to reduce the long-term trend in the piControl run. The cloud-related parameters, such as the relative humidity thresholds for cloud formation and convection, are tuned to reduce the surface temperature drift through changing the energy balance and to simulate better ENSO amplitude through affecting the atmospheric thermodynamic feedback and the oceanic thermocline feedback (Tang et al., 2016; 2019a). Before the frozen FGOALS-g3, some experiments were performed with different coupling intervals for LICOM3, e.g., one day, 6 hours, 3 hours etc. It has been found that 3-hour coupling frequency (i.e., 8 times/day) leads to better ENSO amplitude and smaller climate drift than one day coupling. In addition, it should be noted that the tuning was only focused on the piControl run and there is no tuning for other type runs. The 700-yr mean global average surface temperature (GAST) is 13.7°C with a standard deviation of 0.1°C , and the GAST linear trend is -0.015°C per 100 yr (Fig. 1), which is a smaller climate drift than the CMIP5 piControl run (-0.039°C per 100 yr; Nie et al., 2019). The sea ice extent trend is 397

km²/yr (0.026‰/yr) in the Arctic and 83 km²/yr (0.005‰/yr) in the Antarctic (Figure not shown).

2.3 Data

For FGOALS-g3, the climatological mean of the six member ensemble mean from 1980 to 2014 in the historical runs is used to represent the mean states. The daily output of the first historical member from 1980 to 2014 is used to analyze the variability of 10–20 and 30–80 day (MJO) periods. The monthly output of the first historical member from 1950 to 2014 is used to calculate the interannual variability. For comparison, the climatological mean of the five member ensemble mean from 1980 to 2005 in the historical runs by FGOALS-g2 is used to represent the mean states. For interdecadal variability, both the first member historical run from 1920 to 2005 by FGOALS-g3 and FGOALS-g2 and 700-year piControl run by FGOALS-g3 and 900-year piControl run by FGOALS-g2 are used.

For validation, the observational/re-analysis datasets listed in Table 1 are used: Global Precipitation Climatology Project (GPCP; Version 2.3) data (Adler et al., 2003) and Climate Prediction Center Merged Analysis of Precipitation observations (CMAP) (Xie & Arkin, 1997); ERA-Interim re-analysis data provided by the European Centre for Medium-Range Weather Forecasts (ECMWF) (Dee et al., 2011); monthly sea surface temperature (SST) data from the National Oceanic and Atmospheric Administration (NOAA)/National Climatic Data Center (NCDC) Extended Reconstructed SST Version 5 (ERSST v5) (Huang et al., 2017) and Hadley Centre Global Sea Ice and Sea Surface Temperature (HadISST1.1) dataset produced by the Met Office (Rayner et al., 2003); monthly mean sea level pressure produced by the Hadley Center (HadSLP2) (Allan and Ansell, 2006); surface temperature dataset HadCRUT4 (Morice et al., 2012); monthly sea ice data retrieved with a Bootstrap algorithm from the Scanning Multichannel Microwave Radiometer (SMMR), Special Sensor Microwave/Imager (SSM/I), and Special Sensor Microwave Imager/Sounder (SSMIS) (Comiso, 2017); land temperature data collated by the University of Delaware from a large number of stations (Willmott & Matsuura, 2001), Global Historical Climate Network and the archive of Legates and Willmott (1990); and Global Land Data Assimilation System Version 2 (GLDAS 2) (Rodell et al., 2004).

3. Analyses and evaluations

In this section, the climatological mean state of different components, climate variability over periods from days to decades, long-term evolution of surface temperature from 1850–2100, and the monsoon are evaluated.

3.1 Climatological mean state

3.1.1 Ocean

Figure 2 shows the SST bias of both FGOALS-g2 and FGOALS-g3. In terms of global statistics, the SST mean bias is slightly reduced by FGOALS-g3, including its horizontal root-mean-square errors (RMSE) for the globe, global mean, and maximal and minimal bias

(1.15, -0.15 , 5.23, and -7.85°C) as compared with those (1.54, -0.65 , 6.16, and -7.64°C) from FGOALS-g2 (also in Lin et al., 2013). The warm pool at $\geq 28^{\circ}\text{C}$ simulated by FGOALS-g3 is more accurate than that from FGOALS-g2 (Lin et al., 2013). However, obvious cold biases are located in the northwestern Pacific between $20\text{--}45^{\circ}\text{N}$ and the Barents Sea, and warm biases are still present in the eastern boundary due to the too small amounts of low-level cloud in FGOALS-g3 (Fig. 2a).

The zonal mean temperature biases in FGOALS-g3 (Fig. 3) are similar to those in FGOALS-g2. However, the salinity biases are different. A fresh bias is found in FGOALS-g2 (Li et al., 2013a) while a salt bias is in FGOALS-g3 for the global zonal mean salinity. There is the strong positive salinity bias at around 40°N . The positive salinity anomaly is due to the positive salinity bias in the Mediterranean Sea. This is because the river routing or the representation of the Strait of Gibraltar have deficiencies in the ocean model (Figure not shown). The structure of Antarctic Intermediate Water (AAIW), defined as the salinity tongue enclosed by the 34.8psu contour, is improved. However, the simulated salinity is saltier than the observed.

The global and Atlantic meridional overturning circulation (GMOC and AMOC) are presented in Fig. 4, and the spatial pattern simulations are similar to the referenced observations (Lumpkin & Speer, 2007). The wind-driven upper layer (~ 500 m) cells are well captured by the model. North Atlantic Deep Water (NADW) can reach at the depth of 3500 m depths and even at the ocean bottom north of 30°N . The maximal NADW is located at ~ 1200 m depth between $35\text{--}40^{\circ}\text{N}$, with a value of 34 Sv. Compared with the observed value at 26.5°N from RAPID (~ 18.5 Sv; Cunningham et al., 2007), the modeled value is overestimated, and is also higher than that from FGOALS-g2. In the Atlantic Ocean, Antarctic Bottom Water (AABW) is mainly limited to south of 30°N , while in the Pacific and Indian oceans, AABW is strong with a value of 20 Sv. Although the AMOC and GMOC are strong in the Atlantic, the meridional heat transport is still smaller than that estimated using observations in the Northern Hemisphere south of 30°N (Ganachaud & Wunsch, 2003). This may be related to the slightly colder water that is transported northward in the upper 200m and warmer water that is transported southward between 200-1500m. The simulated heat transport is larger than observed at $\sim 50^{\circ}\text{N}$. In the Southern Hemisphere, the heat transport is well captured at $\sim 30^{\circ}\text{S}$.

3.1.2 Atmosphere

Figure 5 shows the spatial distribution of annual mean precipitation rate from FGOALS-g3 and the biases of FGOALS-g2 and FGOALS-g3 relative to the CMAP. Generally, the two versions can basically capture the large-scale precipitation features, especially the spatial pattern of precipitation over the tropical region. The globally averaged mean precipitation rate modeled by FGOALS-g3 is 2.74 mm/day, much closer to CMAP (2.66 mm/day) than that (2.82 mm/day) by FGOALS-g2. The biases of FGOALS-g3 are smaller than those of FGOALS-g2 in the tropical region south of the equator, e.g., the eastern Indian and Pacific Ocean, which may be related to the improved SSTs by FGOALS-g3.

However, there is an obvious wet bias in the western Indian Ocean, and too much modeled precipitation in the central Pacific near the equator in FGOALS-g3.

The spatial pattern correlation, root-mean-square difference, and amplitude of variation of different meteorological variables by FGOALS-g2 and FGOALS-g3 are summarized in Taylor diagram (Fig. 6), in which the normalization is through the division of the spatial spread of model simulation by the spatial spread of observation for each single variable on the model grids. Generally, the skills of both FGOALS-g2 and FGOALS-g3 in simulating low level (850 hPa) circulation variables are higher than for high level (200 hPa) variables, and the skills in simulating eastward u-wind are better than for northward v-wind (Fig. 6a). Among the different variables, the variables best correlated with the ERA-interim for both versions are the geopotential height at 500 hPa (z_{500}) and temperature at 850 hPa (t_{850}) (Fig. 6a). When considering the interannual variability, the sea level pressure (psl) is the best simulated variable (Fig. 6b). Overall, FGOALS-g3 has a better ability in both annual mean and interannual variability than FGOALS-g2.

3.1.3 Land

Compared with the observational datasets (Willmott & Matsuura, 2001), the overall spatial distribution of the annual mean land surface temperature is basically simulated by FGOALS-g3 (Fig. 7a–b), although there are still cold biases that cover the regions mostly in the high mountain regions (e.g., the Tibetan Plateau) and the near-Arctic region in the Russia and northern Europe. The magnitude of cold bias in FGOALS-g3 is smaller than that in FGOALS-g2 (Fig. 7c), especially in the Northern hemisphere and the Andes in the Southern hemisphere. The improvement in the high mountain and near Arctic region may be associated with the improvement of the snow parametrization.

Figure 8 shows the difference in mean soil water content between MAM and SON between the model simulation and GLDAS2 (Rodell et al., 2009). In general, the simulation agrees with the observations in spatial distribution (Fig. 8a–b). However, in the regions of the Amazon, southern–central Africa, North America, southern–eastern Asia, and Australia, the magnitude of the simulation is smaller than that of GLDAS2, which indicates weaker seasonal variations in the simulated soil water content. The hydrology and snow parameterization schemes in the land surface model may be largely responsible for these biases.

3.1.4 Sea ice

The spatial distributions of annual mean sea ice concentration of FGOALS-g3 compared to the observations of SMMR and SSM/I-SSMIS are shown in Figure 9. In detail, the simulated sea ice is in reasonable agreement with the observations in the Arctic Basin and Antarctic coastal areas. However, in the Arctic, the model produces excess ice along the Eurasian continent and Greenland, including in the Barents Sea, Siberia Sea, Greenland Sea, and Baffin Bay. In the Antarctic, the ice edge in the West Antarctic is more equator-ward but

has a lower sea ice concentration, while in the Indian Ocean sector the simulated sea ice is less than the observations.

3.2 Climate variability

3.2.1 10–20-day variability

The quasi-biweekly (QBW) oscillation (usually referred to as the 10–20-day oscillation) is a high-frequency component of the intra-seasonal oscillation, which can affect both tropical and subtropical weather and short-term mean climate, or even lead to extreme flooding and heat wave events. QBW events are highly concentrated over the East Asia and Western North Pacific (WNP) regions during the boreal summer (Kikuchi & Wang, 2009; Jia & Yang, 2013).

Figure 10 shows the spatial distribution of the 10–20-day outgoing longwave radiation (OLR) variance in early (April–June) and late (July–September) summer during 1980–2014. The Bay of Bengal (BOB), South China Sea (SCS), and WNP are the three large-variance areas, according to NOAA OLR observations (Fig. 10a and d). QBW oscillations over the SCS and WNP show a 7° northward shift (13 to 20°N) from early to late summer with the variance intensity increasing from 250 to 450 W² m⁻⁴, which is consistent with the analysis by Wang and Zhang (2019). The FGOALS-g3 model can simulate the three active QBW oscillation regions in early summer, but with different amplitude variations (Fig. 10a–b). In late summer, the strong QBW oscillation center shows a northward shift in the simulation with the center located east of Taiwan Island, which exhibits a position deviation compared with the observation (Fig. 10d–e). In addition, compared with early summer, the amplitudes of QBW variations in late summer are further underestimated in the three active regions with biases of >–200 W² m⁻⁴ (Fig. 10c and f). Therefore, it remains a challenge for FGOALS-g3 to reasonably simulate such high frequency components of intra-seasonal oscillations in subtropical regions.

3.2.2 MJO

Figure 11 shows the wavenumber–frequency power spectra averaged from 10°S–10°N for OLR and U850 during the boreal winter (November–March). The observed spectral power of OLR and U850 are concentrated over the domain of eastward wavenumbers 1–3 and periods of 30–80 days, which are referred to as the “MJO band” hereafter. The simulated spectral power also shows prominent signals over the MJO band, but the magnitudes are much weaker than the observations. For a quantitative evaluation of the model simulation, the E/W and E/O ratios were calculated. The E/W ratio is defined by dividing the sum of spectral power over the MJO band by that of its westward propagating counterpart. The E/O ratio is obtained by dividing the sum of spectral power of the simulation over the MJO band by the observed value. These two metrics reflect the robustness of the eastward propagating feature of the simulated MJO, and have been frequently used in model evaluation studies (e.g., Lin et al., 2006; Ahn et al., 2017). The observed (simulated) E/W ratio is ~3.7 and ~3.8 (1.9 and 3.4) for OLR and U850, respectively. Furthermore, the E/O ratio is 0.4 for OLR and 0.8 for U850.

This suggests that the model mainly underestimates the eastward propagation of convection, but captures well the eastward propagation of circulation. This is consistent with the CMIP5 model results (Ahn et al., 2017).

Although some deficiencies are detectable in the power spectra diagram of FGOALS-g3, it shows a significant improvement as compared with its previous version (i.e., FGOALS-g2), in which the E/W ratios are ~ 2 for OLR and U850, and the E/O ratio is ~ 0.2 for OLR and 0.5 for U850 (Table 2). Compared with the CMIP5 model results, the performance of FGOALS-g3 is above the average level of the CMIP5 models. The improvement of MJO in FGOALS-g3 could be mainly attributed to the inclusion of convective momentum transport and the modification of boundary layer scheme in GAMIL3 and further enhanced by the atmosphere-ocean coupling process.

Figure 12a–b show the winter lag–longitude diagram of correlation coefficients between 20–100-day filtered OLR and U850 along the equator (10°S – 10°N) versus the 20–100-day filtered OLR over a reference region (10°S – $5^{\circ}\text{N}/75$ – 100°E). In order for negative OLR anomalies to indicate enhanced convection anomalies, the sign of the OLR reference time-series was reversed before calculating the correlation. The observed MJO convection propagated eastward from the Indian Ocean to the dateline, showing a quadrature phase relationship with U850 (Fig. 12a). The eastward propagation of convection can be detected in the simulation, but the signals over the western Pacific are weaker than the observations. The quadrature phase relationship between the convection and zonal wind is well simulated (Fig. 12b).

Figure 12c–d show the summer lag–latitude diagram of correlation coefficients between 20–100-day filtered OLR and U850 along the Bay of Bengal (80 – 100°E) versus the OLR reference time-series. Continuous northward propagation of convection is evident from the equator to 20°N in the observations, with an easterly anomaly to the north of the convection and a westerly anomaly to the south (Fig. 12c). In the simulation, the continuous northward propagation of convection only reaches 10°N , and the asymmetric zonal wind anomalies relative to the convective center are not as clear as the observations (Fig. 12d).

3.2.3 Interannual variability

This section focuses mainly on the simulation of the El Niño–Southern Oscillation (ENSO), Indian Ocean Dipole (IOD), and Atlantic Niño, which are the prominent interannual variabilities in the three tropical basins.

Figure 13a–b show the spatial pattern of the standard deviation of the interannual SST anomaly over the tropical Pacific. The simulated SST anomaly shows large interannual variability in the central and eastern equatorial Pacific, indicating FGOALS-g3 captures the observed spatial distribution of ENSO. From a spatial perspective, the simulated ENSO variability is comparable to that which is observed. Specifically, the standard deviation of the Niño3 index is 0.88 K for the observations and 0.99 K for the FGOALS-g3 simulation (Table 3), indicating a reasonable simulation of the ENSO amplitude. The power spectrum of the observed Niño3 index is characterized by a broad peak ranging from 2–7 years, while the

simulated spectrum is characterized by a single peak at ~ 3 yr (Table 3). These differences in ENSO periodicity simulation may have been inherited from its predecessors (FGOALS-g1 and FGOALS-g2) in which the power of the dominant ENSO frequency is too strong and the bandwidth of the dominant frequency is too narrow (Chen et al., 2016). FGOALS-g3 also exhibits bias in reproducing the observed positive skewness (Table 3), indicating that the simulated ENSO asymmetry is underestimated. This underestimation of ENSO asymmetry remains prevalent in current coupled models (Zhang & Sun, 2014; Tang et al., 2019 b). The phase-locking characteristic of the ENSO cycle (i.e., ENSO-related SST anomalies usually peak during the boreal winter) is reproduced well by FGOALS-g3 (Fig. 13c–d).

Figure 14a–b show the standard deviation of the interannual SST anomaly over the tropical Atlantic and Indian Ocean basins. In general, the spatial pattern of the interannual variability of SST anomalies over the tropical Atlantic and Indian oceans is reproduced by FGOALS-g3. In the tropical Indian Ocean, the IOD simulated by FGOALS-g3 has a slightly stronger amplitude than the observations. Specifically, the standard deviation of SST anomalies averaged over the IODW and IODE are 0.31 and 0.35 K for the observations, but 0.40 and 0.56 K for the simulation. The overestimated IOD amplitude is clearly evident from the time-series of the dipole mode index (DMI; Fig. 14c–d). The IOD amplitude simulation bias is small compared with the majority of CMIP3 and CMIP5 coupled models, which yield an overly larger IOD amplitude (Cai & Cowan, 2013; Liu et al., 2014). The DMI time-series also show that the IOD simulated by FGOALS-g3 exhibits irregular oscillations as observed. Moreover, the phase-locking feature of IOD (i.e., IOD-related SST anomalies usually peak during the boreal autumn) is captured well by FGOALS-g3 (Fig. 14g). In the tropical Atlantic Ocean, the observed and simulated amplitude of the Atlantic Niño are 0.48 and 0.41 K (Table 3), respectively, which shows it is well simulated by FGOALS-g3. As indicated by the Atlantic Niño3 index (Fig. 14e–f), the Atlantic Niño reproduced by FGOALS-g3 exhibits reasonably irregular oscillations as is observed. However, FGOALS-g3 has a bias in duplicating the phase-locking behavior of Atlantic Niño (i.e., Atlantic Niño-related SST anomalies usually peak during June–July; Fig. 14h).

3.2.4 Inter-decadal variability

The Pacific Decadal Oscillation (PDO) and Atlantic Multidecadal Oscillation (AMO) are two important modes of inter-decadal climate variability, which have significant impacts on regional and global climate. In this section, the performance of FGOALS-g3 in simulating the spatial and temporal characteristics of the PDO and AMO is evaluated against the observational datasets.

The PDO index was calculated here as the leading principal component (PC1) of the 9-year low-pass filtered annual SST anomalies over the North Pacific (20–70°N). The global warming signal was removed by subtracting the linear trend before the EOF analysis. The regression shows a characteristic horseshoe-shaped pattern in the North Pacific, with negative anomalies from the Kuroshio–Oyashio extension (KOE) to the central North Pacific and positive anomalies along the west coast of North and South America and tropical central–eastern Pacific during a positive PDO phase (Fig. 15a–b). The spatial pattern is reversed

during a negative PDO phase. The explained variance for the PDO pattern is 42% and 45% in the ERSST and HadISST, respectively. FGOALS-g2 is one of the CMIP5 models which show reasonable performance in simulating the observed PDO pattern (Zhou et al., 2014; Wang and Miao, 2018). The leading EOF (EOF1) patterns, i. e., the PDO, derived from the historical and piControl runs of the FGOALS-g2 explain 56% and 30% of the total variance, respectively (Fig. 15g–h). Compared with the observations, the EOF1 derived from the historical and piControl runs of FGOALS-g3 shows the horseshoe-shaped positive SST anomalies over the North Pacific (Fig. 15 c–d). However, the positive SST anomalies over the Bering Sea are notably overestimated. Meanwhile, the negative SST anomalies from KOE to the central North Pacific are nearly absent in the EOF1 but instead show in the EOF2 patterns (Fig. 15 e–f). The explained variance of the first two EOF modes are 53% and 17% in the historical run, and 37% and 16% in the piControl run. Furthermore, the EOF2 patterns derived from the FGOALS-g3 are similar to the EOF1 patterns derived from the FGOALS-g2 (Fig. 15e–h).

Further analysis of the power spectra of the PDO index derived from ERSST indicates two significant spectral peaks of 10~15 years and ~25 years, while only the longer peak is significant in the HadISST (Fig. 16 a-b). The PC1 time series derived from the historical and piControl runs of the FGOALS-g2 well reproduce the observed spectral peaks (Fig. 16g-h). Due to the longer time coverage of the piControl runs, the power spectra derived from the historical runs look more similar to the observations. In the FGOALS-g3, both the PC1 and PC2 derived from the historical run and piControl run, respectively, reasonably simulate the two spectral peaks of the observed PDO (Fig. 16 c-f). However, the PC1 of the FGOALS-g3 piControl run also shows a significant spectral peak at a longer time period (~50 yr).

The AMO index is defined as the area average of detrended annual SST anomalies over the North Atlantic (80°W – $0^{\circ}/0^{\circ}$ – 60°N). The detrending is performed by subtracting the global mean SST anomaly time-series as suggested in a previous study (Trenberth & Shea, 2006). Considering the multi-decadal timescale of the AMO, the HadISST dataset that covers a longer time period was used as the observations. The regression pattern derived from the HadISST dataset has a characteristic “comma” shape, with large amplitude SST anomalies over the sub-polar regions, along the west coast of north Africa, and over the subtropical North Atlantic (Fig. 17a). The historical run of the FGOALS-g2 reasonably simulates the spatial pattern of the AMO (Fig. 17d), as also indicated in previous study (Lin et al., 2019). However, the positive SST anomalies over the west of Greenland and the Labrador Sea in the piControl run of FGOALS-g2 are overestimated as compared with the observations (Fig. 17e). In the FGOALS-g3, both the historical and piControl simulations reproduce the overall warming over the North Atlantic with relatively large anomalies over the sub-polar regions (Fig. 17b–c). However, the positive SST signals over the Labrador Sea are also overestimated. Moreover, a significant negative SST bias is evident in the Gulf Stream. The AMO pattern by FGOALS-g3 is comparable to but slightly worse than that simulated by FGOALS-g2 (Fig. 17d–e). The power spectra of the observed AMO index peaks at 70–80 yr (Fig. 17f). Power spectral analyses of the AMO index derived from the historical run of FGOALS-g3 broadly reproduce the dominant time period (Fig. 17g), which shows a better performance than the

FGOALS-g2 (Fig. 17i). The power spectra of the 700-yr piControl run of FGOALS-g3 peaks at a period of 20–40 year (Fig. 17h).

3.3 Evolution of SAT in historical and scenario runs

The time-series of the global surface temperature anomalies from the historical and four future scenario runs are shown in Fig. 18, and compared with observations during the historical period. During the historical period, the ensemble mean of the FGOALS-g3 simulations reproduces the general features of the increase in the globally averaged annual mean surface temperature. The warming trends during the periods 1910–1940 and 1970–2005, as well as the cooling trend during the period 1940–1970, are simulated better by FGOALS-g3 than FGOALS-g2 (Table 4). In the FGOALS-g3, the improvement of the warming trends may be associated with the use of the external forcings of CMIP6 that are quite different from those of CMIP5 (Nie et al., 2019). The cooling trend in observation is mainly due to the natural external forcing (e.g., solar irradiation and natural aerosols) and/or internal variability associated with atmosphere-ocean interactions (Thompson et al., 2008; Wang & Dickinson, 2013). Based on the Detection and Attribution Model Intercomparison Project (DAMIP) by FGOALS-g3, the cooling trends are found mainly from the natural forcing experiments (hist-nat) and partly from the aerosol forcing experiments (hist-aer). Taking into account that the cooling trend could not be correctly reproduced by FGOALS-2 with CMIP5 and CMIP6 forcings (Nie et al., 2019), the obvious cooling trend in FGOALS-g3 could be related to its internal variability. However, the relationship between the model improvement and internal variability is needed for further analysis. The future projections of FGOALS-g3 adopted a new set of scenarios produced with six integrated assessment models (IAMs), based on different SSPs according to CMIP6. The global mean surface temperature anomalies projected by FGOALS-g3 under SSP1-2.6 (the updated RCP2.6 pathway; the low end of the range of future forcing pathways in the IAM literature), SSP2-4.5 (the updated RCP4.5 pathway; the medium scenario of the range of future forcing pathways), SSP3-7.0 (a new RCP pathway; a combination of moderate social vulnerability and radiative forcing), and SSP5-8.5 (the updated RCP8.5 pathway; the high end of the range of future pathways in the IAM literature) from FGOALS-g3 are also shown in Fig. 18b. Under the SSP1-2.6 scenario, the global mean surface temperature increases very slowly during 2016–2085, and exhibits a slight decrease during 2085–2100. By 2100, the temperature is comparable to the present-day. Under the other scenarios, all the projections show continuous warming trends, and increases in surface temperature by 2100 relative to 1960–1990 of 1.8°C, 3.2°C, and 3.5°C, respectively. Compared with other three Chinese CMIP6 projections, the warming in FGOALS-g3 is middle among them, positively correlated with their model equilibrium climate sensitivity (ECS) (Zhou et al., 2020). The ECS of FGOALS-g3 is 2.8°C, within the range of 2.27°C~4.65°C for four Chinese CMIP6 models (Fig. 9 in Zhou et al., 2020).

3.4 Monsoon evaluation

The global monsoon domain and precipitation annual range simulated by FGOALS-g3 were firstly evaluated using GPCP as the observations (Fig. 19). Three sub-monsoon systems are clearly present in the observations, including the African, Asian–Australian, and American monsoons where there are large annual ranges in precipitation (Fig. 19a). The observed global monsoon domain and the distribution of annual range are generally well captured by FGOALS-g3, but with some biases (Fig. 19b). The pattern correlation and root-mean-square error of FGOALS-g3 against the observations are 0.73 and 2.3 mm/day, respectively. The simulation is close to those (0.76 and 1.51 mm/day) of FGOALS-g2 (Zhou et al., 2014). From the difference between FGOALS-g3 and GPCP in simulating the annual range of precipitation (Fig. 19c), a systematic weaker monsoon intensity is simulated over the northern hemisphere with a negative bias over the northern African, Indian, Southeast Asian, and North American monsoon regions. The main bias is seen over the Asian–Australian monsoon region, with a smaller area in the Indian monsoon region and relatively larger area in the Northwestern Pacific (NWP) monsoon region. The former bias is caused by the dry bias for the Indian monsoon, which is a common bias in CMIP5 models (Sperber et al., 2013; Zhang et al., 2018). This bias also existed for FGOALS-g2. The latter bias is different from that of FGOALS-g2, which showed a smaller monsoon area in the NWP (Zhou et al., 2014), suggesting an improvement of FGOALS-g3 in simulation of NWP monsoon precipitation.

The performance of FGOALS-g3 on simulating the East Asian summer monsoon (EASM) was further examined. For the climatological mean of precipitation in East Asia (Fig. 20a), FGOALS-g3 has evident dry biases over south–eastern China and the Korean peninsula (Fig. 20e). The mei-yu rain band over the Yangtze River valley (western part of black box in Fig. 20a) is largely missing in the FGOALS-g3 simulation (Fig. 20c), whereas rainfall is overestimated in the eastern Tibetan Plateau and South China Sea. The pattern correlation coefficient (PCC) of rainfall in the east Asian domain is only 0.67. Such rainfall biases already existed in FGOALS-g2 (Zhou et al., 2014), indicating limited improvement in EASM rainfall in the new version. However, the low-level EASM circulation in FGOALS-g3, in contrast to the rainfall deficit, is stronger than the observations (Fig. 20f), with an enhanced WNP Subtropical High (WNPSH), similar to the biases of FGOALS-g2. Thus, the rainfall biases cannot be explained by those of the circulation. Low-level moisture in FGOALS-g3 is evidently underestimated throughout nearly all of the east Asian region, especially over the continent, consistent with the lower rainfall. However, more rainfall over the eastern Tibetan Plateau and South China Sea can be attributed to the stronger monsoon circulation in FGOALS-g3 (Fig. 20f).

Given that the WNPSH is the dominant system in the EASM, the interannual variability of the EASM was evaluated by comparing the anomalous patterns of JJA precipitation and 850 hPa wind associated with a WNPSH index between FGOALS-g3 and the observations. The WNPSH index is defined as a meridional shear of zonal wind between the domain 22–32°N/110–140°E and 5–15°N/100–130°E following Wan and Fan (1999). FGOALS-g3 simulates well the EASM interannual variability, especially for the circulation anomalies with a PCC of 0.96 in the east Asian domain (Fig. 21b), which is better than FGOALS-g2 with a PCC of 0.89 (Zhou et al., 2014). The precipitation pattern is also reproduced and

characterized by dry anomalies in the South China Sea and WNP, and relatively wet anomalies in the maritime continent and meiyu/baiu/changma region (the black box in Fig. 20a). The biases in anomalous circulation are very small, whereas the positive biases in rainfall are evident over the South China Sea, while negative biases characterize the meiyu/baiu/changma region (Fig. 21c). Considering the similar biases of the rainfall interannual anomalies to those of the climatology (Fig. 20e), the underestimation of moisture by FGOALS-g3 (Fig. 20f) may also contribute to the biases in the rainfall interannual variability (Fig. 21c).

Interaction between the EASM and ENSO is one of the most important sources of monsoon interannual variability. Here, the lead–lag correlation coefficient between the Niño3.4 index and JJA WNPSH index is analyzed. It shows that FGOALS-g3 can capture the interaction that an anomalous anticyclone over the WNP is driven by a decaying El Niño from the previous year, which then drives a La Niña in the next winter (Fig. 21d). The effect of decaying El Niño on the summer WNPSH is underestimated in FGOALS-g3, whereas the effect of WNPSH on the developing La Niña is overestimated (Fig. 21d).

4. Summary and Discussion

By upgrading the atmosphere, ocean, and land model components, as well as the coupler, FGOALS-g3 was developed, which was used to conduct the main experiments designed for CMIP6. The performance of FGOALS-g3 was evaluated based on the 700-yr piControl, six member historical, and four member SSPs runs. The results indicate that there are many significant improvements in FGOALS-g3 compared with FGOALS-g2.

Firstly, the simulated climate mean states of many different components, such as sea/land surface temperatures, seasonal cycles of soil moisture and Arctic sea ice concentration (not shown), air temperatures, and geopotential heights are improved. These improvements may be attributed to the reduction of systematic cold biases in FGOALS-g2, due to increasing the resolution, improving the parameterization of physical processes in the component models, and tuning the model repeatedly and carefully for a better piControl run. Beside the parameters in GAMIL3 and LICOM3, the coupling intervals of ocean model component are tuned for a better ENSO and smaller drift in piControl run. The results of this run indicate a smaller climate drift in FGOALS-g3 than in FGOALS-g2, with a more reasonable estimation of the globally averaged climate mean surface temperature for the pre-industrial era of 13.7°C (Fig. 1).

Secondly, FGOALS-g3 captures well some characteristics of climate variability at different scales, e.g., the E/W ratios for OLR and U850 in MJO (Fig. 11), quadrature phase relationship between convection and zonal wind in MJO (Fig. 12), spatial distribution and phase-locking of ENSO and IOD (Figs 13–14), and the dominant timescale of AMO (Fig. 17). In addition, the EASM interannual variability and interaction between EASM and ENSO are well simulated, perhaps related to the strong ENSO and/or interannual variability in FGOALS-g3.

Thirdly, FGOALS-g3 better models the evolution of globally averaged temperature than FGOALS-g2 during the historical period, including closer-to-observation warming trends

during 1910–1940 and 1970–2005, and the cooling trend from 1940–1970 (Fig. 18; Table 3). The improvement in simulating the warming trends is mainly due to the external forcing changes (Nie et al., 2019), while the cooling trend was associated with the internal variability. Except the SSP1-2.6 scenario, the other scenarios (SSP2-4.5, SSP3-7.0 and SSP5-8.5) show continuous warming with the values of 1.8°C, 3.2°C, and 3.5°C by 2100 relative to 1960–1990, respectively.

Fourthly, unlike other CMIP6 models, the anthropogenic groundwater exploitation forcing from 1965–2014 was added to FGOALS-g3, which mainly includes the withdrawal from groundwater pumping and widespread done to supplement human water demand. It has shown that the irrigation resulting from groundwater consumption may increase local evapotranspiration and decrease the temperatures near the surface and in the lower troposphere by affecting soil moisture content (Zou et al., 2014; Zeng et al., 2017). Increased water vapor resulting from groundwater irrigation can also induce local convection and further alter atmospheric water balances (Haddeland et al., 2006; Lo and Famiglietti, 2013). The effect of anthropogenic groundwater exploitation may be more apparent in the severe groundwater extraction region (e.g. northern India, northern China plain, and central United States), although further analysis of the groundwater exploitation is needed to quantify its impacts on the FGOALS-g3 simulations.

Moreover, there are still some obvious biases in FGOALS-g3, and some of these are similar to its previous versions, such as the zonal mean ocean temperature biases (Fig. 3), underestimations of MJO eastward propagation (Figs 12–13), weaker monsoon intensity in the northern hemisphere (Fig. 19), and biases in EASM rainfall (Fig. 20). Some of these biases are even larger than in FGOALS-g2 (e.g., ENSO amplitude–period and rainfall RMSE). Another notable bias of FGOALS-g3 is its performance in simulating the spatial pattern of the PDO (Fig.15). Compared with the observation, biases are also witnessed in simulating fluctuations of the associated Aleutian low pressure system, indicating crucial role of air-sea interactions over the North Pacific for the PDO. However, the PDO is a combined phenomenon influenced by different processes and the root cause of it is still unclear (Newman et al., 2016). An understanding of the model’s performance in simulating the PDO deserves dedicated research in the future. Therefore, FGOALS-g development needs to be continued. In addition, the specific reasons for the many improvements in FGOALS-g3 need to be further investigated, especially with regards to the cooling trend during 1940–1970.

Acknowledgements

The University of Delaware temperature data were provided by the NOAA/OAR/ESRL PSD, Boulder, Colorado, USA (<https://www.esrl.noaa.gov/psd/>). This research was jointly funded by the National Natural Science Foundation of China (Grants 41622503, 41775101, 1605061, 41530426, and 91958201) and a National Key Research Project (Grant 2016YFB0200805). We thank Stephen Griffies and three anonymous reviewers for the helpful comments that improved the manuscript.

The simulated datasets used in this study are archived at the State Key Laboratory of Numerical Modeling for Atmospheric Sciences and Geophysical Fluid Dynamics (LASG),

Institute of Atmospheric Physics, Chinese Academy of Sciences, and are available for research purposes through ESGF-node (<https://esgf-node.llnl.gov/projects/cmip6/>); for details please contact ljli@mail.iap.ac.cn referencing this paper. The coupled model source codes could be obtained after filling out the related memorandum (http://www.lasg.ac.cn/news/202004/t20200425_553389.html), and its atmospheric model codes could be downloaded from the sites <https://doi.org/10.5281/zenodo.3774655>.

Accepted Article

References

- Adler, R. F., Huffman, G. J., Chang, A., Ferraro, R., Xie., P., Janowiak, J., et al. (2003). The version-2 global precipitation climatology project (GPCP) monthly precipitation analysis (1979–present). *Journal of Hydrometeorology*, 4, 1147–1167.
[https://doi.org/10.1175/1525-7541\(2003\)004<1147:tvgps>2.0.co;2](https://doi.org/10.1175/1525-7541(2003)004<1147:tvgps>2.0.co;2)
- Ahn, M. S., Kim, D., Sperber, K. R., Kang, I. S., & Hendon, H. (2017). MJO simulation in CMIP5 climate models: MJO skill metrics and process-oriented diagnosis. *Climate Dynamics*, 49, 4023–4045. <https://doi.org/10.1007/s00382-017-3558-4>
- Allan, R., & Ansell, T. (2006). A new globally complete monthly historical gridded mean sea level pressure dataset (HadSLP2): 1850–2004. *Journal of Climate*, 19, 5816–5842.
<https://doi.org/10.1175/JCLI3937.1>
- Bao, Q., Lin, P. F., Zhou, T. J., Liu, Y. M., Yu, Y. Q., & Wu, G. X. (2013). The Flexible Global Ocean–Atmosphere–Land System model, Spectral Version 2: FGOALS-s2. *Advances in Atmospheric Sciences*, 30(3), 561–576. <https://doi.org/10.1007/s00376-012-2113-9>
- Briegleb, B., & Light, B. (2007). A Delta–Eddington multiple scattering parameterization for solar radiation in the sea ice component of the Community Climate System Model. *NCAR Technical Note*.
- Cai, W., & Cowan, T. (2013). Why is the amplitude of the Indian Ocean Dipole overly large in CMIP3 and CMIP5 climate models? *Geophysical Research Letters*, 40(6), 1200–1205.
<https://doi.org/10.1002/grl.50208>
- Canuto, V. M., Howard, A., Cheng, Y., & Dubovikov, M. S. (2001). Ocean turbulence. Part I: One-point closure model—Momentum and heat vertical diffusivities. *Journal of Physical Oceanography*, 31(6), 1413–1426.
[https://doi.org/10.1175/1520-0485\(2001\)031<1413:OTPIOP>2.0.CO;2](https://doi.org/10.1175/1520-0485(2001)031<1413:OTPIOP>2.0.CO;2)
- Canuto, V. M., Howard, A., Cheng, Y., & Dubovikov, M. S. (2002). Ocean turbulence. Part II: Vertical diffusivities of momentum, heat, salt, mass, and passive scalars. *Journal of Physical Oceanography*, 32(1), 240–264.
[https://doi.org/10.1175/1520-0485\(2002\)032<0240:otpivd>2.0.co;2](https://doi.org/10.1175/1520-0485(2002)032<0240:otpivd>2.0.co;2)
- Chen, K. M., Zhang, X. H., Lin, X. Z. J., & Lin, W. Y. (1997). A coupled ocean–atmosphere general circulation model for global climate change study, Part I: The model’s configuration and performance. *Acta Oceanologica Sinica*, 19(3), 21–32. (In Chinese)
- Chen, L., Yu, Y. Q., & Zheng, W. (2016). Improved ENSO simulation from climate system model FGOALS-g1.0 to FGOALS-g2. *Climate Dynamics*, 47(7–8), 2617–2634.
<https://doi.org/10.1007/s00382-016-2988-8>
- Comiso, J. C. (2017). Bootstrap Sea Ice Concentrations from Nimbus-7 SMMR and DMSP SSM/I-SSMIS, Version 3. Boulder, Colorado USA. NASA National Snow and Ice Data Center Distributed Active Archive Center. doi: <https://doi.org/10.5067/7Q8HCCWS4I0R>.

- Covey, C., Achutarao, K. M., Cubasch, U., Jones, P., Lambert, S. J., Mann, M. E., et al. (2003). An overview of results from the Coupled Model Intercomparison Project. *Global and Planetary Change*, 37(1–2), 103–133. [https://doi.org/10.1016/S0921-8181\(02\)00193-5](https://doi.org/10.1016/S0921-8181(02)00193-5)
- Craig, A. P., Jacob, R., Kauffman, B., Bettge, T., Larson, J., Ong, E., et al. (2005). CPL6: The new extensible, high-performance parallel coupler for the Community Climate System Model. *International Journal for High Performance Computing Applications*, 19(3), 309–327. <https://doi.org/10.1177/1094342005056117>
- Craig, A. P., Vertenstein, M., & Jacob, R. (2012). A new flexible coupler for earth system modeling developed for CCSM4 and CESM1. *International Journal for High Performance Computing Applications*, 26(1), 31–42. <https://doi.org/10.1177/1094342011428141>
- Cunningham, S. A., Kanzow, T. O., Rayner, D., Barringer, M. O., Johns, W. E., Marotzke, J., et al. (2007). Temporal variability of the Atlantic meridional overturning circulation at 26.5°N. *Science*, 317(5840), 935–938. <https://doi.org/10.1126/science.1141304>
- Eyring, V., Bony, S., Meehl, G. A., Senior, C. A., Bjorn, S., Stouffer, R. J., & Taylor, K. E. (2016). Overview of the Coupled Model Intercomparison Project Phase 6 (CMIP6) experimental design and organization. *Geoscientific Model Development*, 9(5), 1937–1958. <https://doi.org/10.5194/gmd-9-1937-2016>
- Ferreira, D., Marshall, J., & Heimbach, P. (2005). Estimating eddy stresses by fitting dynamics to observations using a residual-mean ocean circulation model and its adjoint. *Journal of Physical Oceanography*, 35(10), 1891–1910. <https://doi.org/10.1175/JPO2785.1>
- Ganachaud, A., & Wunsch, C. (2003). Large-scale ocean heat and freshwater transports during the world ocean circulation experiment. *Journal of Climate*, 16(4), 696–705. [https://doi.org/10.1175/1520-0442\(2003\)016<0696:LSOHAF>2.0.CO;2](https://doi.org/10.1175/1520-0442(2003)016<0696:LSOHAF>2.0.CO;2)
- Gao, J., Xie, Z., Wang, A., & Luo, Z. (2016). Numerical simulation based on two-directional freeze and thaw algorithm for thermal diffusion model. *Applied Mathematics and Mechanics*, 37(11), 1467–1478. <https://doi.org/10.1007/s10483-016-2106-8>
- Gao, J., Xie, Z. H., Wang A. W., Liu, S., Zeng, Y. J., Liu, B., et al. (2019). A new frozen soil parameterization including frost and thaw fronts in the Community Land Model. *Journal of Advances in Modeling Earth System*, 11(3), 659–679. <https://doi.org/10.1029/2018MS001399>
- Gent, P. R., & McWilliams, J. C. (1990). Isopycnal mixing in ocean circulation models. *Journal of Physical Oceanography*, 20(1), 150–155. [https://doi.org/10.1175/1520-0485\(1990\)020<0150:IMIOCM>2.0.CO;2](https://doi.org/10.1175/1520-0485(1990)020<0150:IMIOCM>2.0.CO;2)
- Guo, Z., & Zhou, T. (2014) An improved diagnostic stratocumulus scheme based on estimated inversion strength and its performance in GAMIL2. *Science China Earth Sciences*, 57(11), 2637–2649. <https://doi.org/10.1007/s11430-014-4891-7>
- Haddeland, I., D. P. Lettenmaier, & Skaugen, T. (2006). Effects of irrigation on the water and energy balances of the Colorado and Mekong River basins. *Journal of Hydrology*, 324, 210–223. <https://doi.org/10.1016/j.jhydrol.2005.09.028>

- Hunke, E. C., & Dukowicz, J. K. (1997). An elastic–viscous–plastic model for sea ice dynamics. *Journal of Physical Oceanography*, 27, 1849–1867.
[https://doi.org/10.1175/1520-0485\(1997\)027<1849:AEVPMF>2.0.CO;2](https://doi.org/10.1175/1520-0485(1997)027<1849:AEVPMF>2.0.CO;2)
- IPCC (1992). *Climate Change 1992: The Supplementary Report to the IPCC Scientific Assessment*. Houghton, J. T., Callander, B. A., & Varney, S. K. (Eds.). Cambridge University Press, 200 pp.
- IPCC (1996). *Climate Change 1995: The Science of Climate Change*. Houghton, T. J., et al. (Eds.). Cambridge University Press, Cambridge, U.K., 572 pp.
- IPCC (2001). *Climate Change 2001: The Scientific Basis*. Watson, E., Houghton, T. J., & Ding, Y. (Eds.). Cambridge University Press, Cambridge, U.K., 882 pp.
- IPCC (2007). *Climate Change 2007: The Physical Science Basis*. Contribution of Working Group I to the Fourth Assessment Report of the Intergovernmental Panel on Climate Change [Solomon, S., Qin, D., Manning, M., Chen, Z., Marquis, M., Averyt, K. B., Tignor, M., & Miller, H. L. (Eds.)]. Cambridge University Press, Cambridge, United Kingdom and New York, NY, USA, 996 pp.
- IPCC (2013). *Climate change 2013: The Physical Science Basis*. Stocker, T. F., Qin, D. H., Plattner, G. K., Tignor, M. M. B., Allen, S. K. et al. (Eds). Cambridge: Cambridge University Press.
- Jia, X., & Yang, S. (2013). Impact of the quasi-biweekly oscillation over the western North Pacific on East Asian subtropical monsoon during early summer. *Journal of Geophysical Research-Atmosphere*, 118(10), 4421–4434. <https://doi.org/10.1002/jgrd.50422>
- Jochum, M. (2009). Impact of latitudinal variations in vertical diffusivity on climate simulations. *Journal Geophysical Research*, 114, C01010.
<https://doi.org/10.1029/2008JC005030>.
- Jung, M., Reichstein, M., Ciais, P., Seneviratne, S. I., Sheffield, J., Goulden, M. L., et al. (2010). Recent decline in the global land evapotranspiration trend due to limited moisture supply. *Nature*, 467(7318), 951–954. <https://doi.org/10.1038/nature09396>
- Kikuchi, K., & Wang, B. (2009). Global perspective of the quasi-biweekly oscillation. *Journal of Climate*, 22(6), 1340–1359. <https://doi.org/10.1175/2008JCLI2368.1>
- Large, W. G., Danabasoglu, G., Doney, S. C., & McWilliams, J. C. (1997). Sensitivity to surface forcing and boundary layer mixing in a global ocean model: annual-mean climatology. *Journal of Physical Oceanography*, 27(11), 2418–2447.
[https://doi.org/10.1175/1520-0485\(1997\)027<2418:STSFAB>2.0.CO;2](https://doi.org/10.1175/1520-0485(1997)027<2418:STSFAB>2.0.CO;2)
- Larson, J., Jacob, R., & Ong, E. (2005). The model coupling toolkit: A new Fortran90 toolkit for building multiphysics parallel coupled models. *International Journal of High Performance Computing Applications*, 19(3), 277–292.
<https://doi.org/10.1177/1094342005056116>

- Laurent, L. C. S., Simmons, H. L., & Jayne, S. R. (2002). Estimating tidally driven mixing in the deep ocean. *Geophysical Research Letters*, *29*, 2106. <https://doi.org/10.1029/2002GL015633>
- Li, L. J., Lin, P. F., Yu, Y. Q., Wang, B., Zhou, T. J., Liu, L., et al. (2013a). The Flexible Global Ocean–Atmosphere–Land System model, Grid-Point Version 2: FGOALS-g2. *Advances in Atmospheric Sciences*, *30*(3), 543–560. <https://doi.org/10.1007/s00376-012-2140-6>
- Li, L. J., Wang, B., Dong, L., Liu, L., Shen, S., Hu, N., et al. (2013b). Evaluation of grid-point atmospheric model of IAP LASG Version 2 (GAMIL2). *Advances in Atmospheric Sciences*, *30*(3), 855–867. <https://doi.org/10.1007/s00376-013-2157-5>
- Lin, J. L., Kiladis, G. N., Mapes, B. E., Weickmann, K. M., Sperber, K. R., Lin, W. Y., et al. (2006). Tropical intraseasonal variability in 14 IPCC AR4 climate models. part I: convective signals. *Journal of Climate*, *19*, 2665–2690. <https://doi.org/10.1175/JCLI3735.1>
- Lin, P. F., Liu, H. L., & Zhang, X. H. (2007). Sensitivity of the upper ocean temperature and circulation in the Equatorial Pacific to solar radiation penetration due to phytoplankton. *Advances in Atmospheric Sciences*, *24*(5), 765–780. <https://doi.org/10.1007/s00376-007-0765-7>
- Lin, P. F., Liu, H. L., Xue, W., Li, H. M., Jiang, J. R., Song, M. R., et al. (2016). A coupled experiment with LICOM2 as the ocean component of CESM1. *Journal of Meteorological Research*, *30*(1), 76–92. <https://doi.org/10.1007/s13351-015-5045-3>
- Lin P. F., Yu Y. Q., & Liu, H. L. (2013). Oceanic Climatology in the Coupled Model FGOALS-g2: Improvements and Biases. *Advances in Atmospheric Sciences*, *30*(3), 819–840. <https://doi.org/10.1007/s00376-012-2137-1>
- Lin, P. F., Yu, Z. P., Lu, J. H., Ding, M. R., Hu, A. X., & Liu, H. L. (2019). Two regimes of Atlantic multidecadal oscillation: cross-basin dependent or Atlantic-intrinsic. *Science Bulletin*, *64*(3), 198–204. <https://doi.org/10.1016/j.scib.2018.12.027>
- Lipscomb, W. H., & Hunke, E. C. (2004). Modeling sea ice transport using incremental remapping. *Monthly Weather Review*, *132*, 1341–1354. [https://doi.org/10.1175/1520-0493\(2004\)132<1341:MSITUI>2.0.CO;2](https://doi.org/10.1175/1520-0493(2004)132<1341:MSITUI>2.0.CO;2)
- Lipscomb, W. H., Hunke, E. C., Maslowski, M., & Jakacki, J. (2007). Ridging, strength, and stability in high-resolution sea ice models. *Journal of Geophysical Research Oceans*, *112*, C03S91. <https://doi.org/10.1029/2005JC003355>
- Liu, H. L., Zhang, X. H., Li, W., Yu, Y. Q., & Yu, R. C. (2004). An eddy-permitting oceanic general circulation model and its preliminary evaluations. *Advances in Atmospheric Sciences*, *21*(5), 675–690. <https://doi.org/10.1007/BF02916365>
- Liu, H. L., Lin, P. F., Yu, Y. Q., & Zhang, X. H. (2012). The baseline evaluation of LASG/IAP Climate System Ocean Model (LICOM) version 2.0. *Acta Meteorologica Sinica*, *26*(3), 318–329. <https://doi.org/10.1007/s13351-012-0305-y>

- Liu, L., Xie, S. P., Zheng, X. T., Li, T., Du, Y., Huang, G., & Yu, W. D. (2014). Indian Ocean variability in the CMIP5 multi-model ensemble: the zonal dipole mode. *Climate Dynamics*, 43(5–6), 1715–1730. <https://doi.org/10.1007/s00382-013-2000-9>
- Liu, L., Zhang, C., Li, R., Wang, B., & Yang, G. (2018). C-Coupler2: a flexible and user-friendly community coupler for model coupling and nesting. *Geoscientific Model Development*, 11, 3557–3586. <https://doi.org/10.5194/gmd-11-3557-2018>
- Liu, S., Xie, Z. H., Zeng, Y. J., Liu, B., Li, R. C., Wang, Y., et al. (2019). Effects of anthropogenic nitrogen discharge on dissolved inorganic nitrogen transport in global rivers. *Global Change Biology*, 25(4), 1–21. <https://doi.org/10.1111/gcb.14570>
- Lo, M. H., & Famiglietti, J. S. (2013). Irrigation in California’s Central Valley strengthens the southwestern U.S. water cycle. *Geophysical Research Letters*, 40, 301–306. <https://doi.org/10.1002/grl.50108>.
- Lumpkin, R., & Speer, K. (2007). Global ocean meridional overturning. *Journal of Physical Oceanography*, 37(10), 2550–2562. <https://doi.org/10.1175/JPO3130.1>
- Madec, G., & Imbard, M. (1996). A global ocean mesh to overcome the north pole singularity. *Climate Dynamics*, 12(6), 381–388. <https://doi.org/10.1007/BF00211684>
- Matthes, K., Funke, B., Andersson, M. E., Barnard, L., Beer, J., Charbonneau, P., et al. (2017). Solar forcing for CMIP6 (v3.2). *Geoscientific Model Development*, 10(6), 2247–2302. <https://doi.org/10.5194/gmd-10-2247-2017>
- Meehl, G. A., Covey, C., McAvaney, B. J., Latif, M., & Stouffer, R. J. (2005). Overview of the Coupled Model Intercomparison Project. *Bulletin of the American Meteorological Society*, 86(1), 89–93. <https://doi.org/10.1175/BAMS-86-1-89>
- Mesinger, F., & Janjic, Z. I. (1985). Problems and numerical methods of the incorporation of mountains in atmospheric models. *Lectures in Applied Mathematics*, 22, 81–120.
- Morice, C. P., Kennedy, J. J., Rayner, N. A. & Jones, P. D. (2012) Quantifying uncertainties in global and regional temperature change using an ensemble of observational estimates: the HadCRUT4 dataset. *Journal of Geophysical Research*, 117, D08101. <https://doi.org/10.1029/2011JD017187>
- Murray, R. J. (1996). Explicit generation of orthogonal grids for ocean models. *Journal of Computational Physics*, 126(2), 251–273. <https://doi.org/10.1006/jcph.1996.0136>
- Newman, M., Alexander, M. A., Ault, T. R., Kobb, K. M., Deser, C. et al. (2016). The Pacific Decadal Oscillation, Revisited. 2. *Journal of Climate*, 29(12), 4399–4427. <https://doi.org/10.1175/JCLI-D-15-0508.1>
- Nie, Y., Li, L. J., Tang, Y. L., & Wang, B. (2019). Impacts of changes of external forcings from CMIP5 to CMIP6 on surface temperature in FGOALS-g2. *SOLA*, 15, 211–215. <https://doi.org/10.2151/sola.2019-038>
- Ohlmann, J. C. (2003). Ocean radiant heating in climate models. *Journal of Climate*, 16, 1337–1351. <https://doi.org/10.1175/1520-0442-16.9.1337>

- Oleson, K., Lawrence, D. M., Bonan, G. B., Drewniak, B., Huang, M., Koven, C. D., et al. (2013). Technical description of version 4.5 of the Community Land Model (CLM). NCAR Tech, Note NCAR/TN-503+STR, 420 pp. <https://doi.org/10.5065/D6RR1W7M>
- Redi, M. H. (1982). Oceanic isopycnal mixing by coordinate rotation. *Journal of Physical Oceanography*, *12*(10), 1154–1158. [https://doi.org/10.1175/1520-0485\(1982\)012<1154:OIMBCR>2.0.CO;2](https://doi.org/10.1175/1520-0485(1982)012<1154:OIMBCR>2.0.CO;2)
- Rodell, M., Houser, P. R., Jambor, U., Gottschalck, J., Mitchell, K., Meng, C. J., et al. (2004). The global land data assimilation system. *Bulletin of the American Meteorological Society*, *85*(3), 381–394. <https://doi.org/10.1175/BAMS-85-3-381>
- Shi, X. J., Zhang, W. T., & Liu, J. J. (2019). Comparison of anthropogenic aerosol climate effects among three climate models with reduced complexity. *Atmosphere*, *10*(18), 456. <https://doi.org/10.3390/atmos10080456>
- Sperber, K. R., Annamalai, H., Kang, I., Kitoh, A., Moise, A. F., Turner, A. G., et al. (2013). The Asian summer monsoon: An intercomparison of CMIP5 vs. CMIP3 simulations of the late 20th century. *Climate Dynamics*, *41*, 2711–2744. <https://doi.org/10.1007/s00382-012-1607-6>
- Stevens, B., Fiedler, S., Kinne, S., Peters, K., Rast, S., Musse, J., et al. (2017). MACv2-SP: A parameterization of anthropogenic aerosol optical properties and an associated Twomey effect for use in CMIP6. *Geoscientific Model Development*, *10*(1), 433–452. <https://doi.org/10.5194/gmd-10-433-2017>
- Sun, W. Q., Li, L. J., & Wang, B. (2016). Reducing the biases in shortwave cloud radiative forcing in tropical and subtropical regions from the perspective of boundary layer processes. *Science China Earth Sciences*, *59*(7), 1427–1439. <https://doi.org/10.1007/s11430-016-5290-z>
- Tang, Y. L., Li, L. J., Dong, W. J., & Wang, B. (2016). Reducing the climate drift in a new coupled model. *Science Bulletin*, *61*(6), 488–494. <https://doi.org/10.1007/s11434-016-1033-y>
- Tang, Y. L., Li, L. J., Wang, B., Lin, P. F., Chen, L., Xie, F., W. J., & Xia, K. (2019a). The dominant role of the atmospheric component of coupled models in ENSO amplitude simulations. *Climate Dynamics*, *52*, 4833–4947. <https://doi.org/10.1007/s00382-018-4416-8>
- Tang, Y. L., Li, L. J., Wang, B., Lin, P. F., Dong, W. J., & Xia, K. (2019b). The collective contribution of atmospheric and oceanic components to ENSO asymmetry. *Atmosphere*, *10*(8), 469. <https://doi.org/10.3390/atmos10080469>
- Thompson, D. W. J., Kennedy, J. J., Wallace, J. M., & Jones, D. Phil. (2008). A large discontinuity in the mid-twentieth century in observed global-mean surface temperature. *Nature*, *453*(7195), 646–649. <https://doi.org/10.1038/nature06982>
- Wang, B., & Fan, Z. (1999). Choice of South Asian summer monsoon indices. *Bulletin of the American Meteorological Society*, *80*(4), 629–638. [https://doi.org/10.1175/1520-0477\(1999\)080<0629:COSASM>2.0.CO;2](https://doi.org/10.1175/1520-0477(1999)080<0629:COSASM>2.0.CO;2)

- Wang, B., & Ding, Q. H. (2008). Global monsoon: Dominant mode of annual variation in the tropics. *Dynamics of Atmospheres and Oceans*, 44(3), 165–183. <https://doi.org/10.1016/j.dynatmoce.2007.05.002>
- Wang, K., & Dickinson, R. E. (2013). Contribution of solar radiation to decadal temperature variability over land. *Proceedings of the National Academy of Sciences of the United States of America*, 110(37), 14877–14882. <https://doi.org/10.1073/pnas.1311433110>
- Wang, T., & Miao, J. P. (2018). Twentieth-century Pacific Decadal Oscillation simulated by CMIP5 coupled models. *Atmospheric and Oceanic Science Letters*, 11(1), 94–101. <https://doi.org/10.1080/16742834.2017.1381548>
- Wang, X., & Zhang, G. (2019). Evaluation of the quasi-biweekly oscillation over the South China Sea in early and late summer in CAM5. *Journal of Climate*, 32(1), 69–84. <https://doi.org/10.1175/jcli-d-18-0072.1>
- Willmott, C. J., & Matsuura, K. (2001). Terrestrial air temperature and precipitation: Monthly and annual time series (1950–1999), http://climate.geog.udel.edu/~climate/html_pages/README.ghcn_ts2.html
- Wu, G. X., Zhang, X. H., Liu, H., Yu, Y. Q., Jin, X. Z., Guo, Y. F., et al. (1997). LASG global ocean–atmosphere–land system model (GOALS/LASG) and its simulation performance. *Quarterly Journal of Applied Meteorological Science*, 8 (Suppl.), 15–28 (in Chinese).
- Wu, X. Q., Deng, L. P., Song, X. L., & Zhang, G. J. (2007). Coupling of convective momentum transport with convective heating in global climate simulations. *Journal of the Atmospheric Sciences*, 64(4), 1334–1349. <https://doi.org/10.1175/JAS3894.1>
- Xiao, C. (2006). Adoption of a two-step shape-preserving advection scheme in an OGCM and its coupled experiment (Master's thesis). Beijing: Institute of Atmospheric Physics, Chinese Academy of Sciences (in Chinese).
- Xie, P. P., & Arkin, P. A. (1997). Global precipitation: A 17-year monthly analysis based on gauge observations, satellite estimates, and numerical model outputs. *Bulletin of the American Meteorological Society*, 78(11), 2539–2558. [https://doi.org/10.1175/1520-0477\(1997\)078<2539:GPAYMA>2.0.CO;2](https://doi.org/10.1175/1520-0477(1997)078<2539:GPAYMA>2.0.CO;2)
- Xie, Z. H., Di, Z. H., Luo, Z. D., & Ma, Q. (2012). A quasi-three-dimensional variably saturated groundwater flow model for climate modeling. *Journal of Hydrometeorology*, 13(1), 27–46. <http://doi.org/10.1175/JHM-D-10-05019.1>
- Xie, Z. H., Liu, S., Zeng, Y. J., Gao, J. Q., Qin, P. H., Jia, B. H., et al. (2018). A high-resolution land model with groundwater lateral flow, water use and soil freeze–thaw front dynamics and its applications in an endorheic basin. *Journal of Geophysical Research Atmospheres*, 123, 7204–7222. <http://doi.org/10.1029/2018JD028369>
- Yu, R. C. (1994). A two-step shape-preserving advection scheme. *Advances in Atmospheric Sciences*, 11(4), 479–490. <http://doi.org/10.1007/BF02658169>

- Yu, Y. Q., & Zhang, X. H. (1998). A modified air–sea flux anomaly coupling scheme. *Chinese Science Bulletin*, 43, 866–870. doi: 10.3321/j.issn:0023-074X.1998.08.019
- Yu, Y. Q., Yu, R. C., Zhang, X. H., & Liu, H. L. (2002). A flexible global coupled climate model. *Advances in Atmospheric Sciences*, 19(1), 169–190. <https://doi.org/10.1007/s00376-002-0042-8>
- Yu, Y. Q., Zhang, X. H., & Guo Y. F. (2004). Global coupled ocean–atmosphere general circulation models in LASG/IAP. *Advances in Atmospheric Sciences*, 21(3), 444–455. <https://doi.org/10.1007/BF02915571>
- Yu, Z. P., Liu, H. L., & Lin, P. F. (2017). A numerical study of the influence of tidal mixing on Atlantic meridional overturning circulation (AMOC) simulation. *Chinese Journal of Atmospheric Sciences*, 41(5), 1087–1100 (in Chinese). <https://doi.org/10.3878/j.issn.1006-9895.1702.16263>
- Yu, R. C. (1994). A two-step shape-preserving advection scheme. *Advances in Atmospheric Sciences*, 11(4), 479–490. <https://doi.org/10.1007/BF02658169>
- Yu, Y. Q., Tang, S. L., Liu, H. L., Lin, P. F., & Li, X. L. (2018). Development and evaluation of the dynamic framework of an ocean general circulation model with arbitrary orthogonal curvilinear coordinate. *Chinese Journal of Atmospheric Sciences*, 42(4), 877–889 (in Chinese). <https://doi.org/10.3878/j.issn.1006-9895.1805.17284>
- Zeng, Y. J., Xie, Z. H., Yu, Y., Liu, S., Wang, L. Y., Jia, B. H., et al. (2016a). Ecohydrological effects of stream–aquifer water interaction: a case study of the Heihe River basin, northwestern China. *Hydrology and Earth System Sciences*, 20(6), 2333–2352. <https://doi.org/10.5194/hess-20-2333-2016>
- Zeng, Y. J., Xie, Z. H., Yu, Y., Liu, S., Wang, L. Y., Zou, J., et al. (2016b). Effects of anthropogenic water regulation and groundwater lateral flow on land processes. *Journal of Advances in Modeling Earth Systems*, 8(3), 1106–1131. <https://doi.org/10.1002/2016MS000646>
- Zeng, Y. J., Xie, Z. H., & Zou, J. (2017). Hydrologic and climatic responses to global anthropogenic groundwater extraction. *Journal of Climate*, 30(1), 71–90. <https://doi.org/10.1175/JCLI-D-16-0209.1>
- Zeng, Y. J., Xie, Z. H., Liu, S., Xie, J. B., Jia, B. H., Qin, P. H., & Gao, J. Q. (2018). Global land surface modeling including lateral groundwater flow. *Journal of Advances in Modeling Earth Systems*, 10(8), 1882–1900. <https://doi.org/10.1029/2018MS001304>
- Zhang, L. X., Zhou, T. J., Klingaman, N. P., Wu, P. L., & Roberts, M. J. (2018). Effect of horizontal resolution on the representation of the global monsoon annual cycle in AGCMs. *Advances in Atmospheric Sciences*, 35(8), 1003–1020. <https://doi.org/10.1007/s00376-018-7273-9>
- Zhang, T., & Sun, D. Z. (2014). ENSO asymmetry in CMIP5 models. *Journal of Climate*, 27(11), 4070–4093. <https://doi.org/10.1175/JCLI-D-13-00454.1>

Zhang, X. H., & Liang, X. Z. (1989). A numerical world ocean general circulation model. *Advances in Atmospheric Sciences*, 6(1), 43–61. <https://doi.org/10.1007/BF02656917>

Zhang, X. H., Bao, N., Yu, R. C., & Wang, W. Q. (1992). Coupling experiments based on an atmospheric and an oceanic GCM. *Chinese Journal of Atmospheric Sciences*, 16, 129–144 (in Chinese).

Zhou, T. J., Chen, X. L., Dong, L., Wu, B., Man, W. M., Zhang, L. X., et al. (2014). Chinese contribution to CMIP5: An overview of five Chinese models' performances. *Journal of Meteorological Research*, 28(4), 481–509. <https://doi.org/10.1007/s13351-014-4001-y>

Zhou, T. J., Chen Z. M., Zou L. W., Chen, X. L., Yu, Y. Q., Wang, B., et al. (2020). Development of Climate and Earth System Models in China: Past Achievements and New CMIP6 Results. *Journal of Meteorological Research*, 34(1), 1–19. <https://doi.org/10.1007/s13351-020-9164-0>

Zou, J., Xie, Z. H., Yu, Y., Zhan, C. S., & Sun, Q. (2014). Climatic responses to anthropogenic groundwater exploitation: a case study of the Haihe River Basin, Northern China. *Climate Dynamics*, 42, 2125–2145. <https://doi.org/10.1007/s00382-013-1995-2>

Zou, J., Xie, Z. H., Zhan, C. S., Qin, P. H., Sun, Q., Jia, B. H., & Xia, J. (2015). Effects of anthropogenic groundwater exploitation on land surface processes: A case study of the Haihe River Basin, Northern China. *Journal of Hydrology*, 524, 625–641. <https://doi.org/10.1016/j.jhydrol.2015.03.026>

Accepted

Table 1. The observational/re-analysis datasets used for comparison.

Datasets	Periods	Reference
Global Precipitation Climatology Project (GPCP; Version 2.3) data	1980–2014	Adler et al., 2003
Climate Prediction Center Merged Analysis of Precipitation observations (CMAP)	1980–2014	Xie & Arkin, 1997
ERA-Interim re-analysis data provided by the European Centre for Medium-Range Weather Forecasts (ECMWF)	1980–2014	Dee et al., 2011
monthly sea surface temperature (SST) data from the National Oceanic and Atmospheric Administration (NOAA)/National Climatic Data Center (NCDC) Extended Reconstructed SST Version 5 (ERSST v5)	1920–2014	Huang et al., 2017
Hadley Centre Global Sea Ice and Sea Surface Temperature (HadISST1.1) dataset produced by the Met Office	1870–2014	Rayner et al., 2003
monthly mean sea level pressure produced by the Hadley Center (HadSLP2)	1870–2014	Allan and Ansell, 2006
surface temperature dataset HadCRUT4	1870–2014	Morice et al., 2012
monthly sea ice data retrieved with a Bootstrap algorithm from the Scanning Multichannel Microwave Radiometer (SMMR), Special Sensor Microwave/Imager (SSM/I), and Special Sensor Microwave Imager/Sounder (SSMIS)	1980–2014	Comiso, 2017
land temperature data collated by the University of Delaware from a large number of stations	1980–2014	Willmott & Matsuura, 2001; Legates & Willmott (1990)
Global Land Data Assimilation System Version 2 (GLDAS 2)	1980–2014	Rodell et al., 2004

Table 2. Statistics for MJO eastward propagation calculated from the historical experimental results based on FGOALS-g3, FGOALS-g2, and CMIP5 multi-model mean (MME). Note that the results for FGOALS-g2 and CMIP5 MME were derived from Fig. 2a and b in Ahn et al. (2017).

	FGOALS-g3		FGOALS-g2		CMIP5 MME	
	OLR	U850	OLR	U850	OLR	U850
E/W ratio	1.9	3.4	2	2	1.9	2.4
E/O ratio	0.4	0.8	0.2	0.5	0.5	0.75

Table 3. The standard deviation, skewness, and period peaks of the Niño3 index, and the standard deviation of the IODW, IODE, and Atlantic Niño3 indexes.

	Niño3 Std (K)	Niño3 Skewness (K)	Niño Period (yr)	IODW Std (K)	IODE Std (K)	Atl3 Std (K)
OBS	0.88	0.64	2~7	0.31	0.35	0.48
FGOALS-g3	0.99	-0.20	3.0	0.40	0.56	0.41

Table 4. Linear trend of global surface temperature anomalies over three periods, which were obtained from observations and the ensemble average (spread) of the historical runs from FGOALS-g2 and FGOALS-g3 (in °C/10 yr).

	Observations	FGOALS-g2	FGOALS-g3
1910–1940	0.140	0.043(0.025~0.055)	0.099(0.073~0.107)
1940–1970	-0.026	0.025(-0.004~0.06)	-0.022(-0.027~0.002)
1970–2005	0.195	0.173(0.153~0.179)	0.176(0.151~0.198)

e

Global average surface temperature

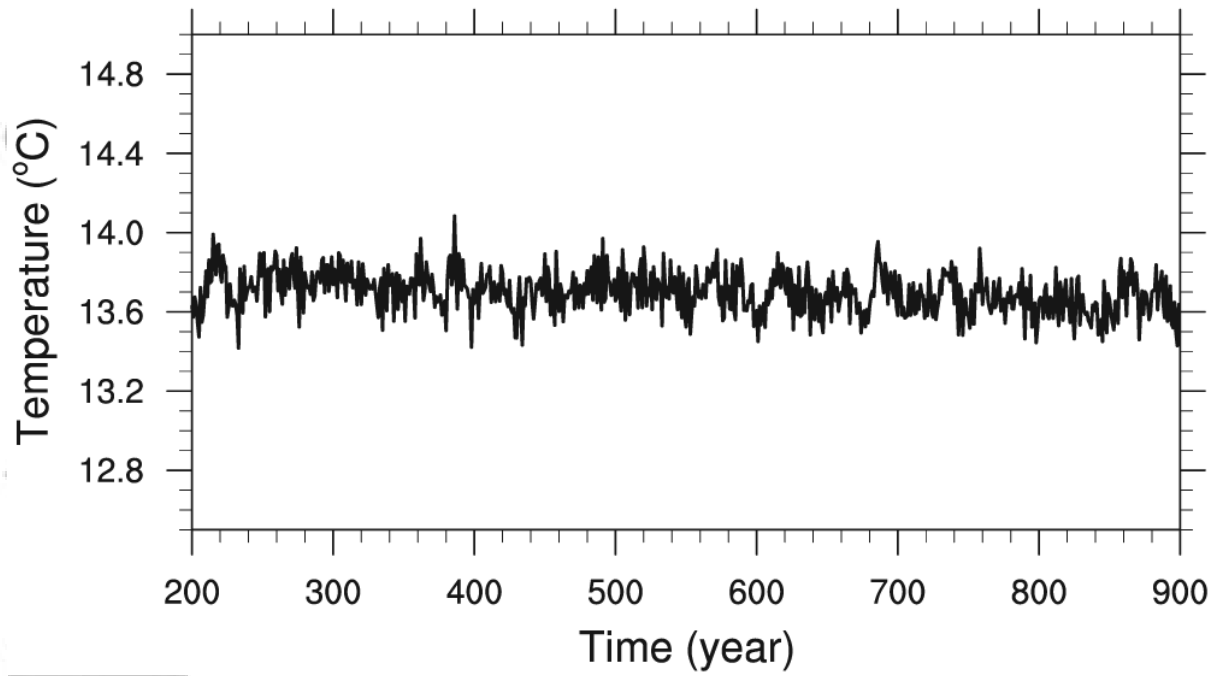


Figure 1. Evolution of globally averaged surface temperature from the 700-year pre-industrial control run by FGOALS-g3.

Accepted

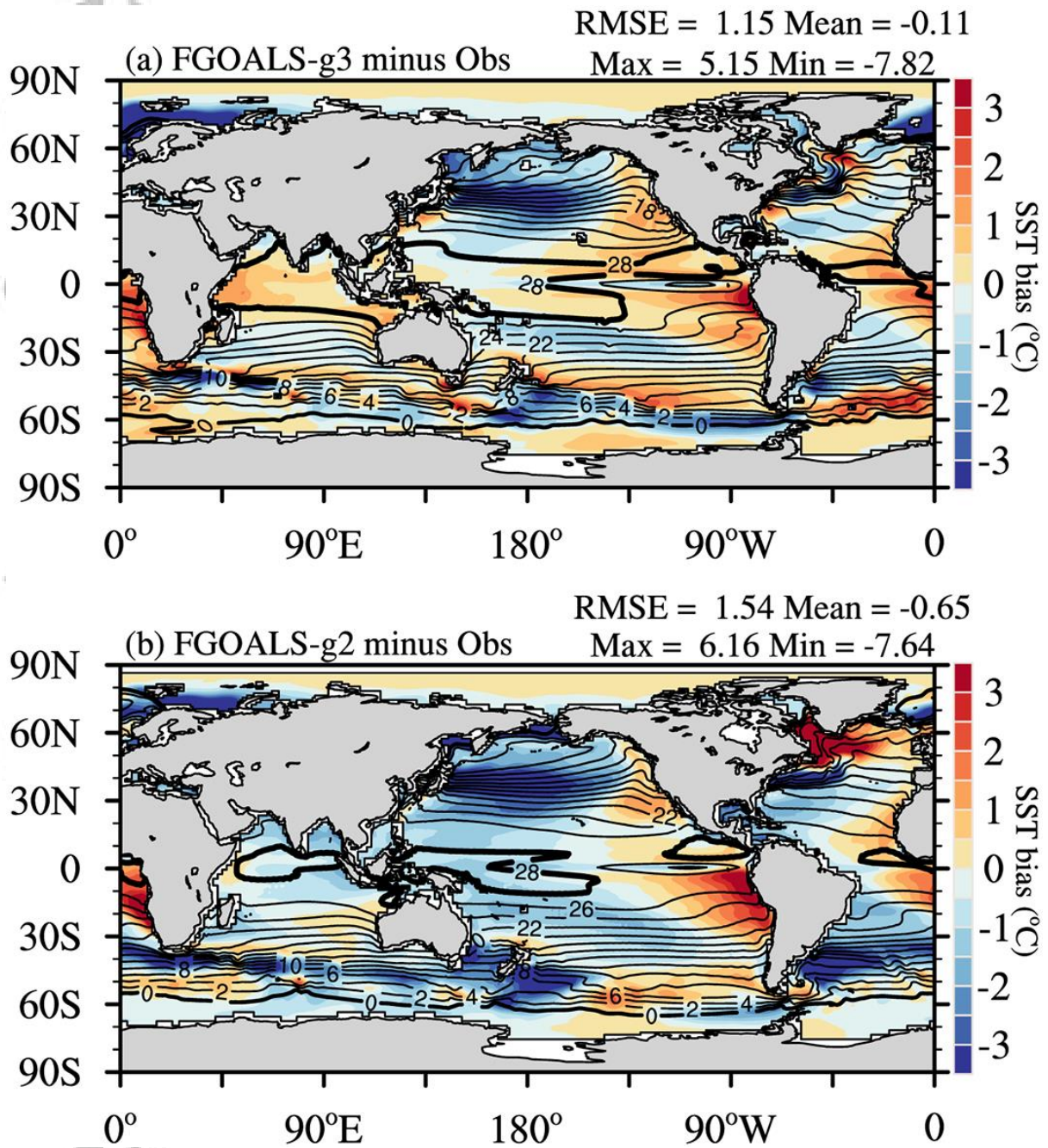


Figure 2. Horizontal distributions of annual mean SST bias (units: °C) (a) from the FGOALS-g3 ensemble mean based on six historical runs and (b) from the FGOALS-g2 ensemble mean based on four historical runs. The ERSSTv5 is referenced as the observed.

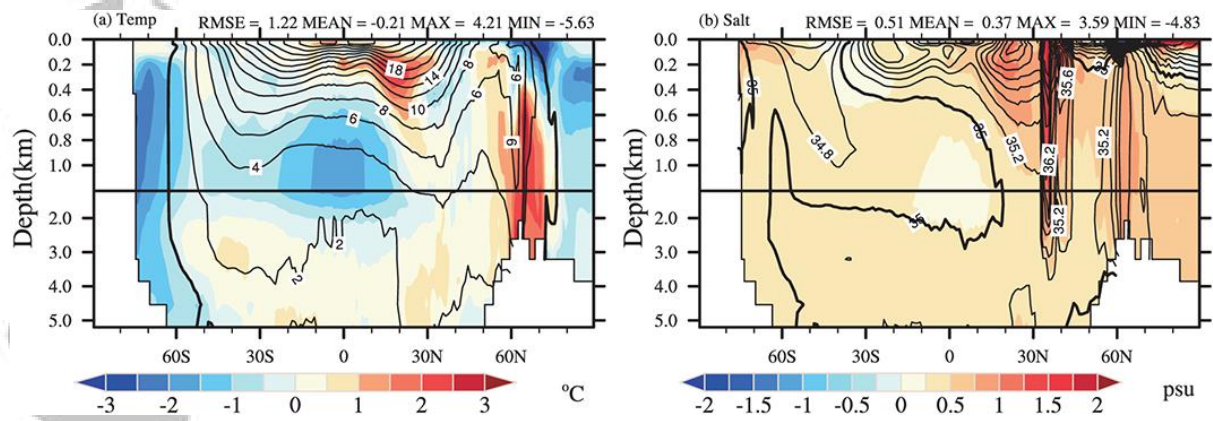


Figure 3. Annual zonal mean (contours) of (a) temperature and (b) salinity, and their biases (colored shading) during 1980–2014 from the ensemble mean based on six historical runs. WOA13 is referenced as the observed. The 0°C and 35 psu contours are shown as thick lines.

Accepted Article

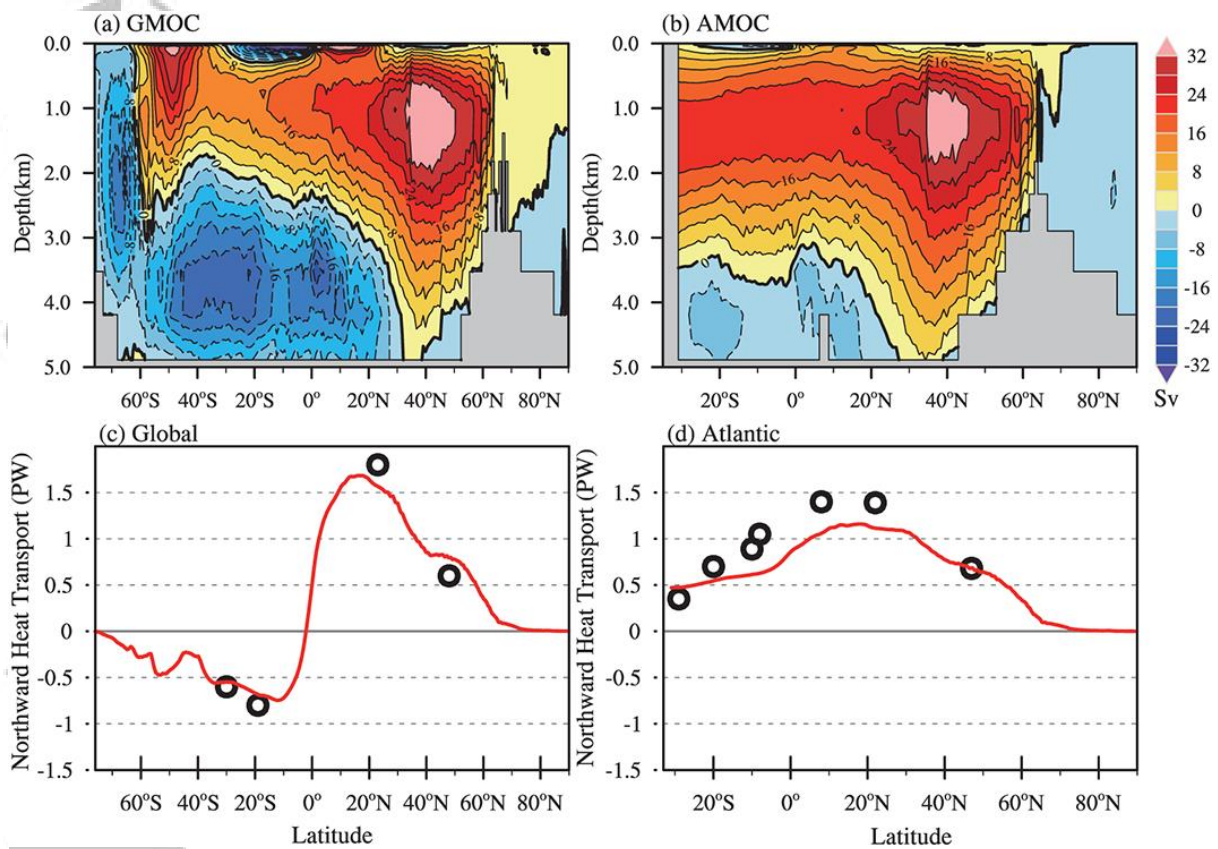


Figure 4. The annual mean states of (a) global and (b) Atlantic meridional overturning circulation (i.e., GMOC and AMOC), and (c) global and (d) Atlantic poleward heat transport (PW; $1\text{PW} = 10^{15} \text{ W}$) during 1980–2014 from the ensemble mean based on six historical runs. The red line shows the ensemble mean and the black dots are the estimates from Ganachaud and Wunsch (2003). The AMOC is only plot north of 32°S due to the unclosed eastern and western boundary of Atlantic Ocean.

Accepted

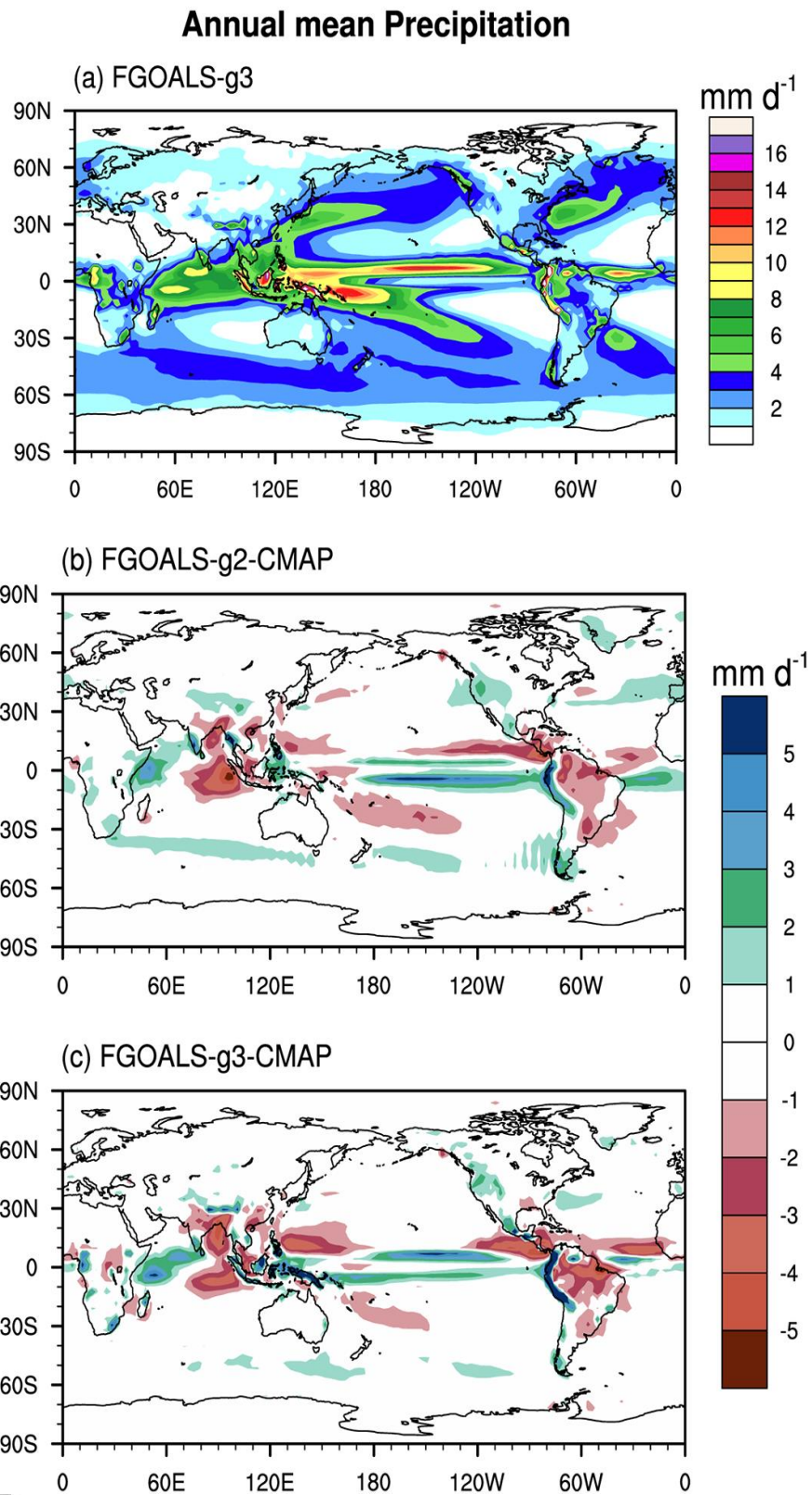


Figure 5. Spatial distribution of annual mean precipitation rate (mm/day) from (a) FGOALS-g3 and the biases of (b) FGOALS-g2 and (c) FGOALS-g2 compared to CMAP .

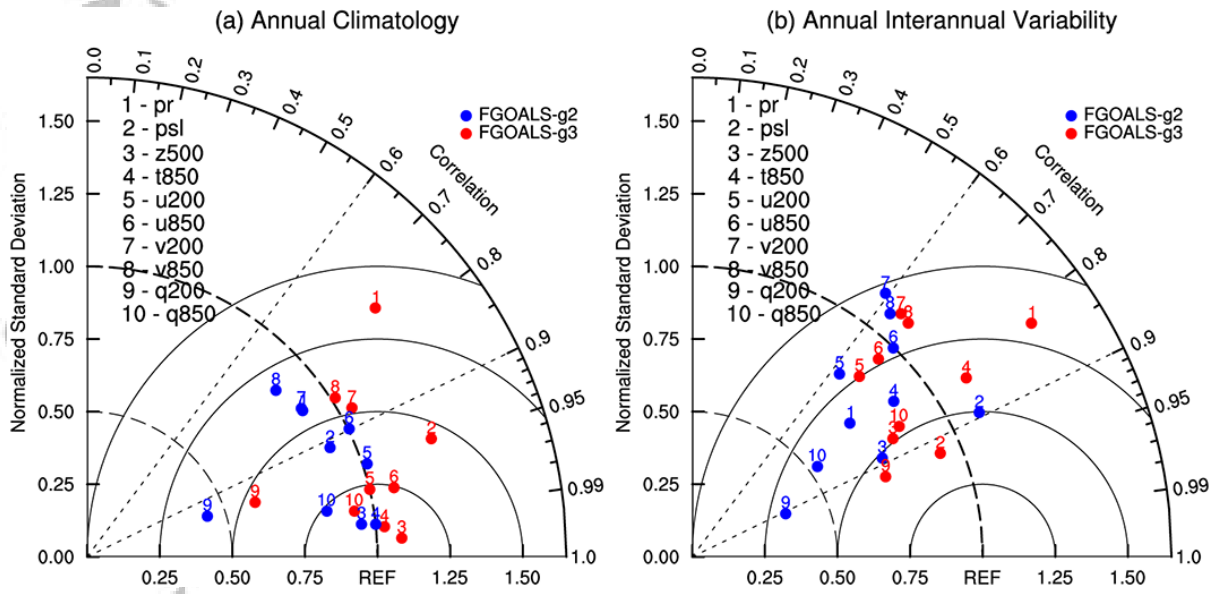


Figure 6. Multivariable Taylor diagram displaying normalized statistical comparisons of FGOALS-g3 (red), and FGOALS-g2 (blue) historical experiment simulated (a) climatology and (b) interannual variability of different meteorological variables with ERA-interim and GPCP as observations, respectively. The numbers represent different variables, which include precipitation (pr), sea level pressure (psl), 500 hPa geopotential height (z500), 850 hPa air temperature (t850), 200 and 850 hPa zonal wind (u200 and u850), 200 and 850 hPa meridional wind (v200 and v850), 200 and 850hPa specific humidity (q200 and q850).

Accepted

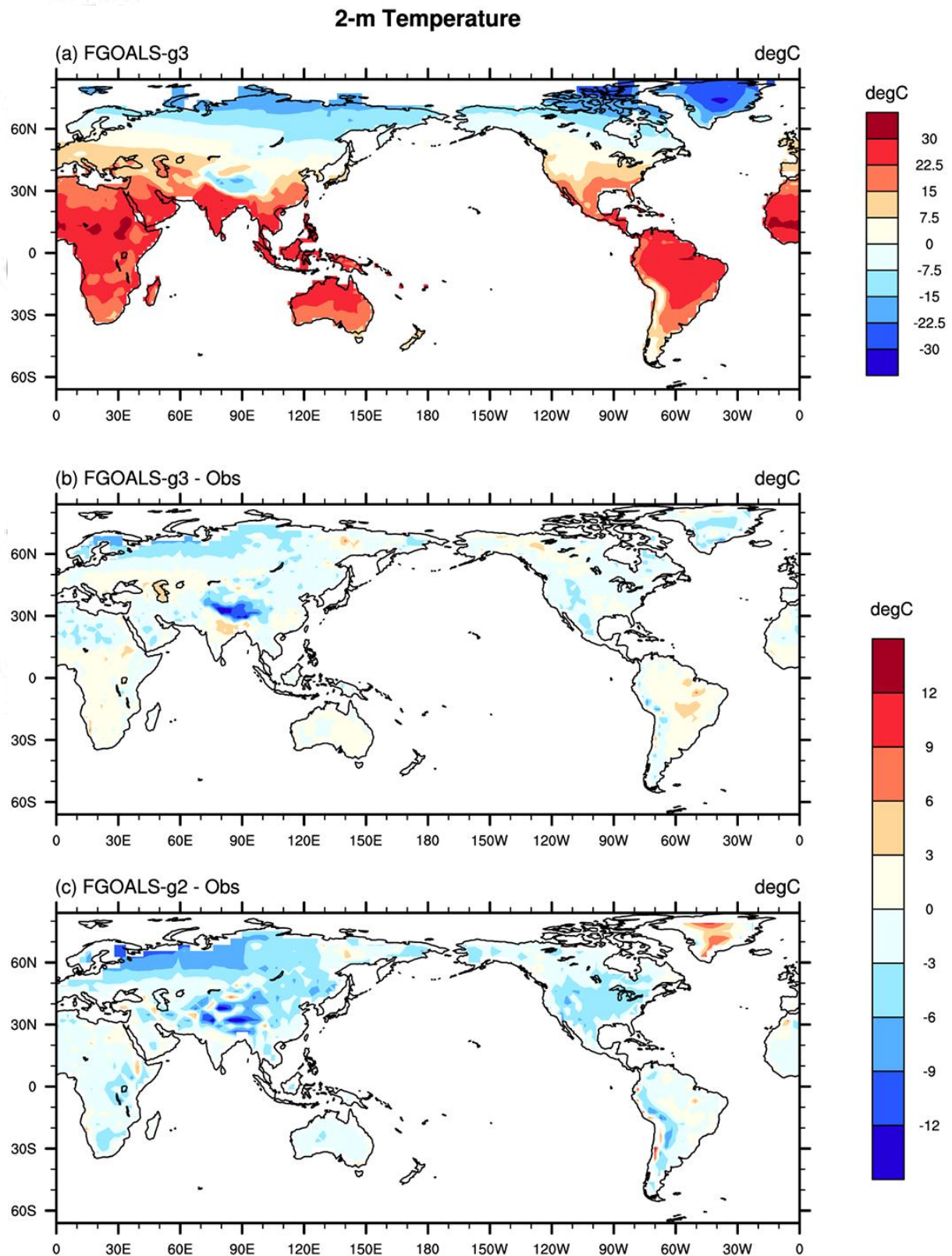


Figure 7. Spatial distribution of 2-m temperature (degC) from (a) FGOALS-g3 and the bias of (b) FGOALS-g3 and (c) FGOALS-g2 compared to Willmott and Matsuura (2001).

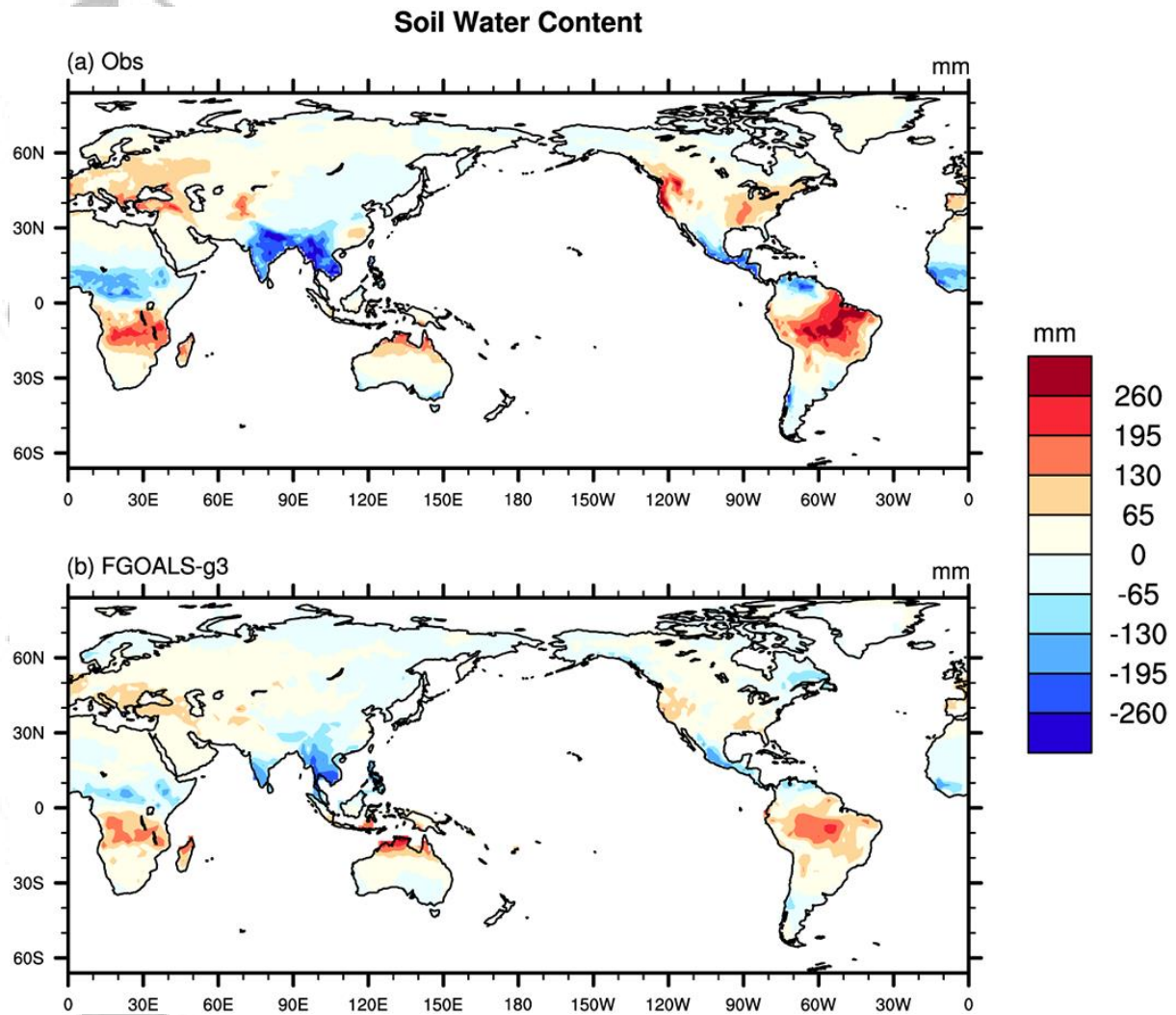


Figure 8. Difference in mean soil water content (mm) between MAM and SON for (a) GLDAS 2 and (b) FGOALS-g3.

Accepted

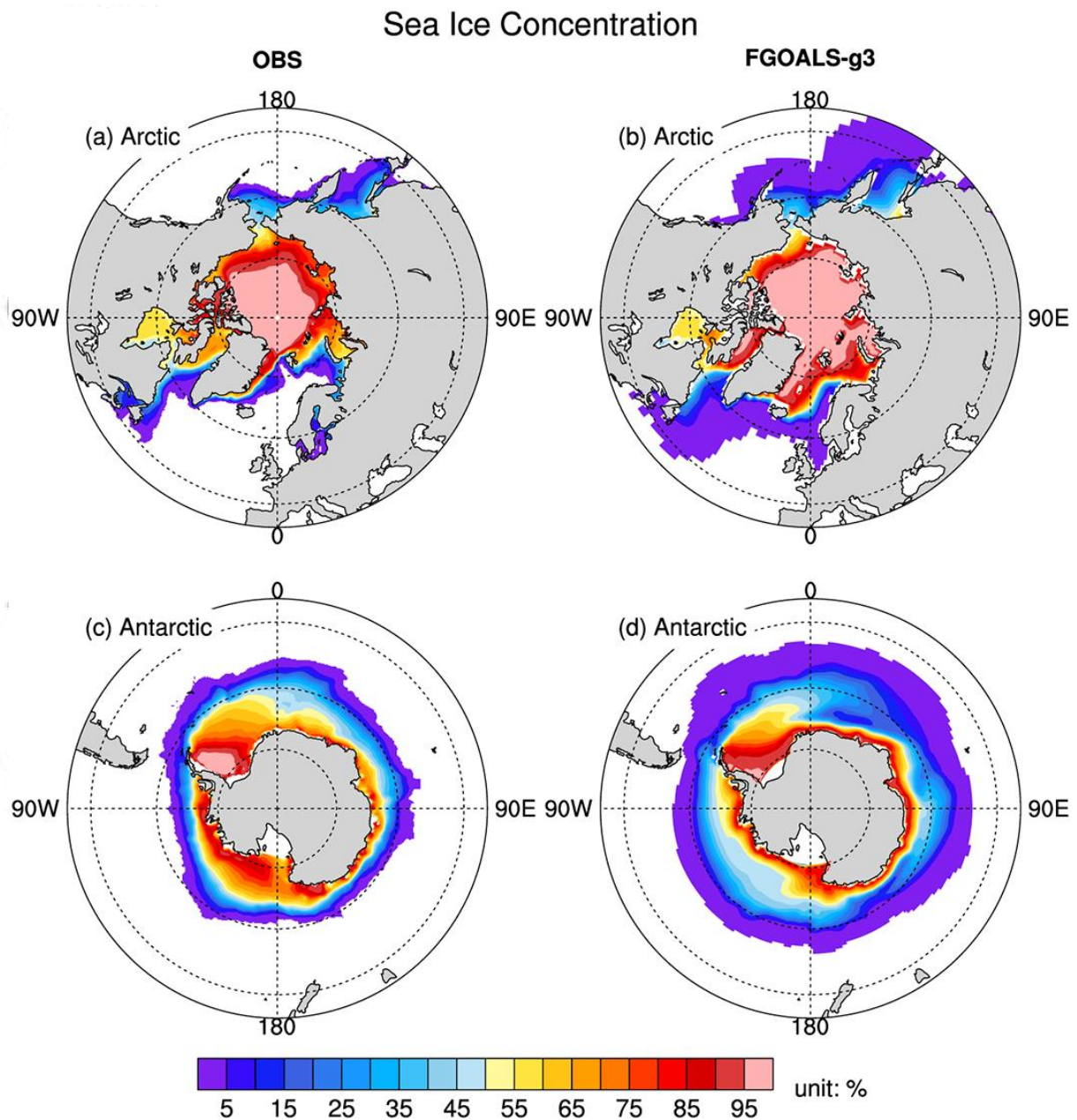


Figure 9. Annual mean (a–b) Arctic and (c–d) Antarctic sea ice concentrations (in %) from the FGOALS-g3 historical ensemble mean run (b, d) and SMMR&SSM/I-SSMIS observations (a, c).

Accepted

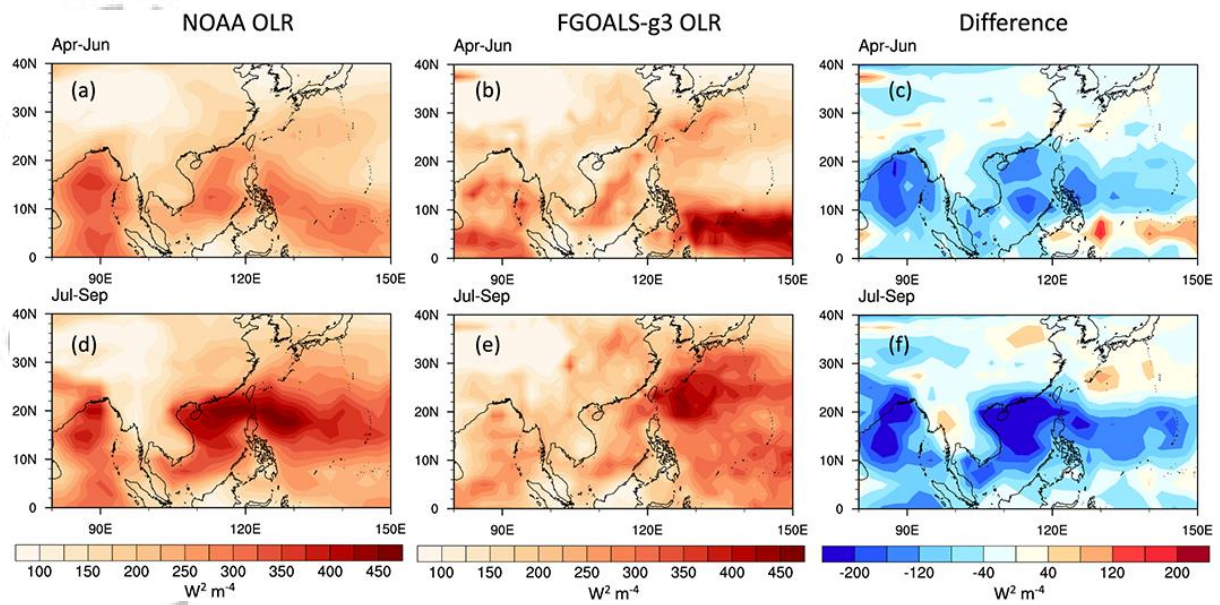


Figure 10. Spatial distribution of 10–20-day OLR variance ($W^2 \text{ m}^{-4}$) from NOAA OLR observations (left) and FGOALS-g3 simulations (middle), and the differences between the model and observations (right) for (a–c) April–June and (d–f) July–September during 1980–2014.

Accepted

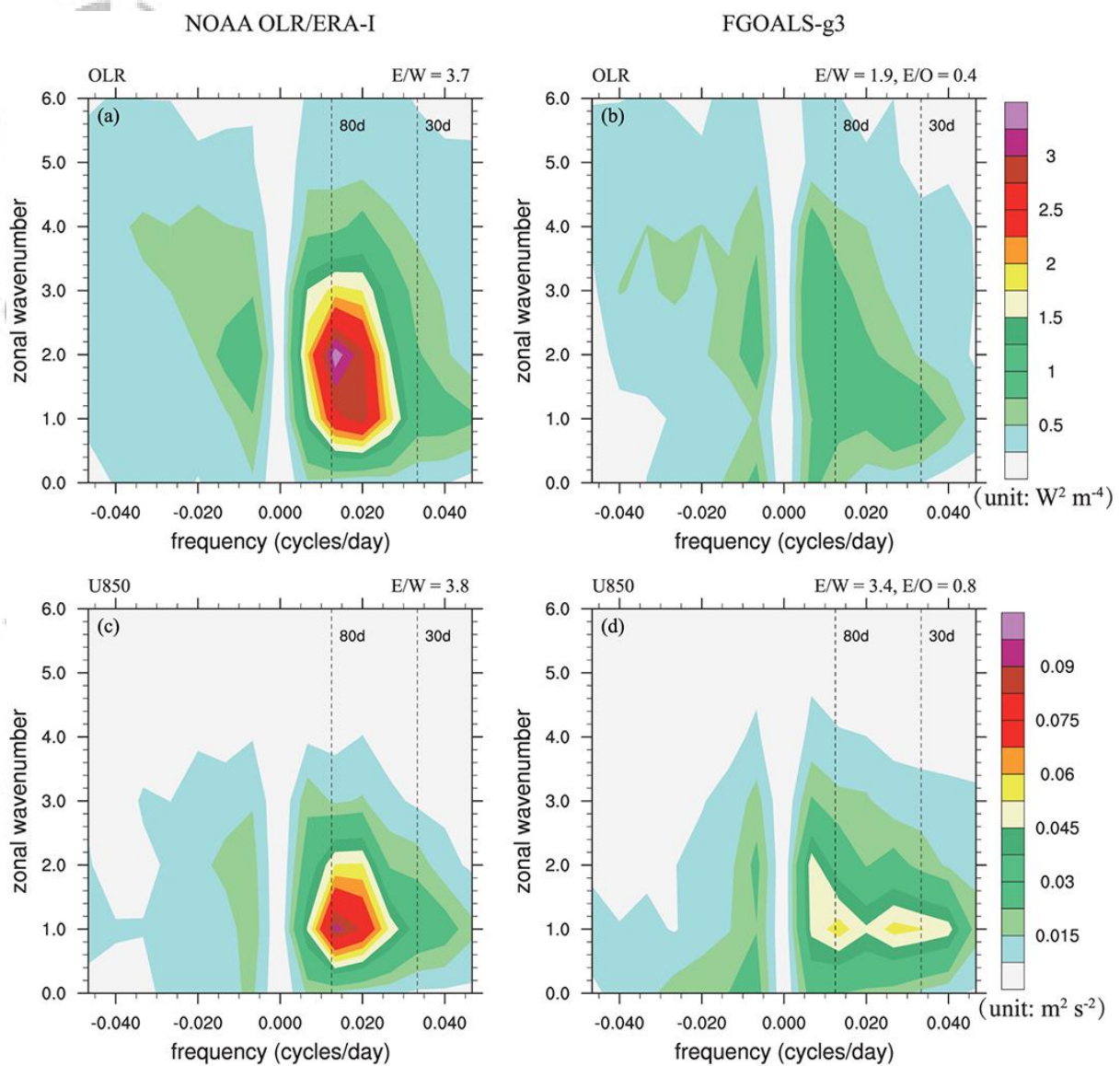


Figure 11. Wavenumber–frequency power spectra averaged for $10^{\circ}S$ – $10^{\circ}N$ for the (a–b) OLR and (c–d) 850 hPa zonal wind in boreal winter (November–March) for observations (left) and the FGOALS-g3 historical simulation (right). Units of the power spectra for the OLR and 850 hPa zonal wind are $W^2 m^{-4}$ and $m^2 s^{-2}$, respectively.

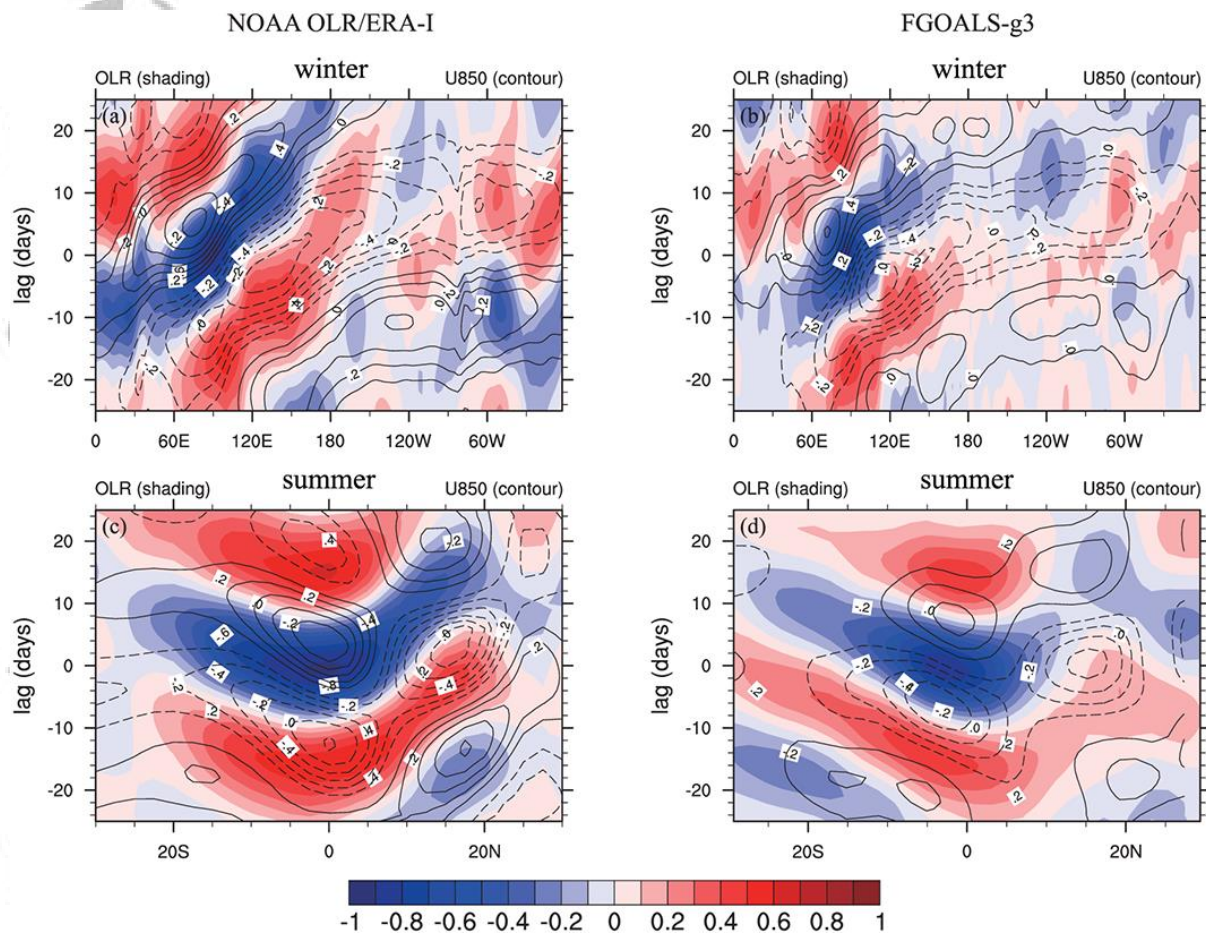


Figure 12. (Upper panels) Boreal winter (November–March) lag-longitude diagram of correlation coefficients between 20–100-day filtered OLR (shaded) and U850 (contours) upon the 20–100-day filtered OLR averaged over a reference region (10° S– 5° N, 75° – 100° E). (Lower panels) Boreal summer (June–October) lag-latitude diagram of correlation coefficients between 20–100-day filtered OLR (shaded) and U850 (contours) upon the same OLR reference time series. Note that the OLR reference time series was reversed sign before calculating correlation. (a) and (c) are for observations while (b) and (d) are for FGOALS-g3 historical simulation.

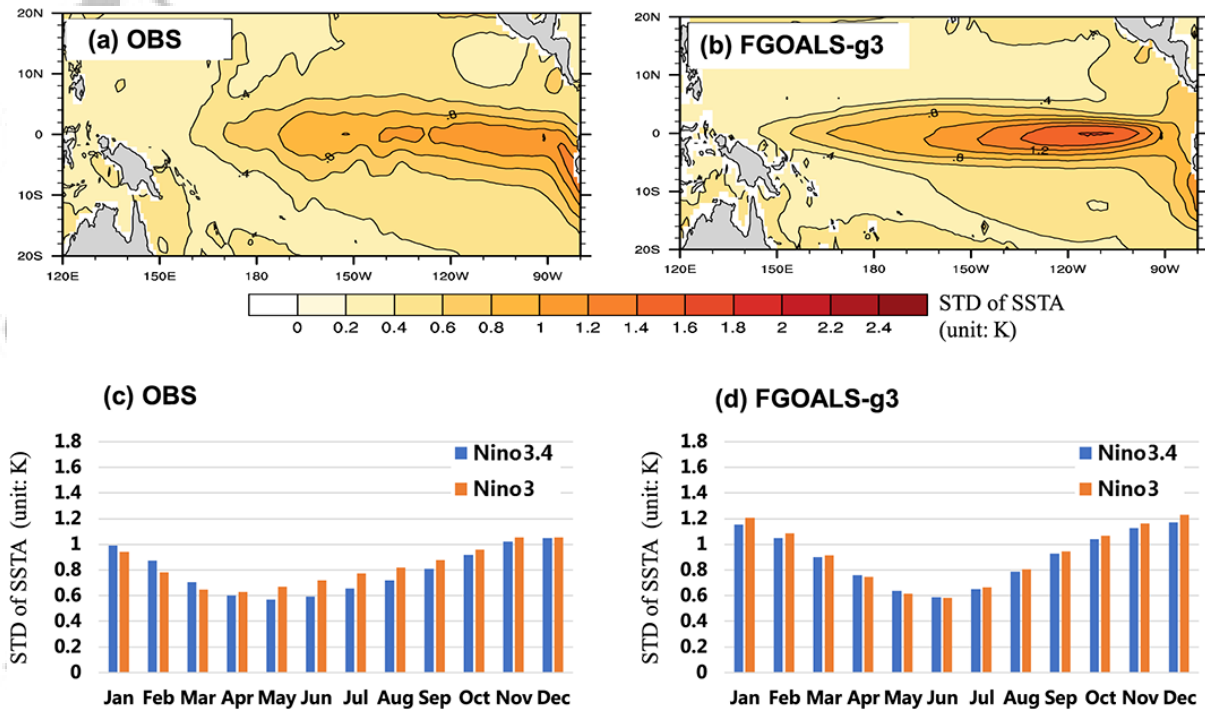


Figure 13. (a–b) Spatial distribution of the standard deviation of the interannual anomaly of SST, derived from the observation (left) and the FGOALS-g3 historical simulation (right). (c–d) Standard deviations of SST anomalies for each calendar month. Orange and blue bars indicate the averaged results over the Niño3 and Niño3.4 regions, respectively. Unit is K.

Accepted

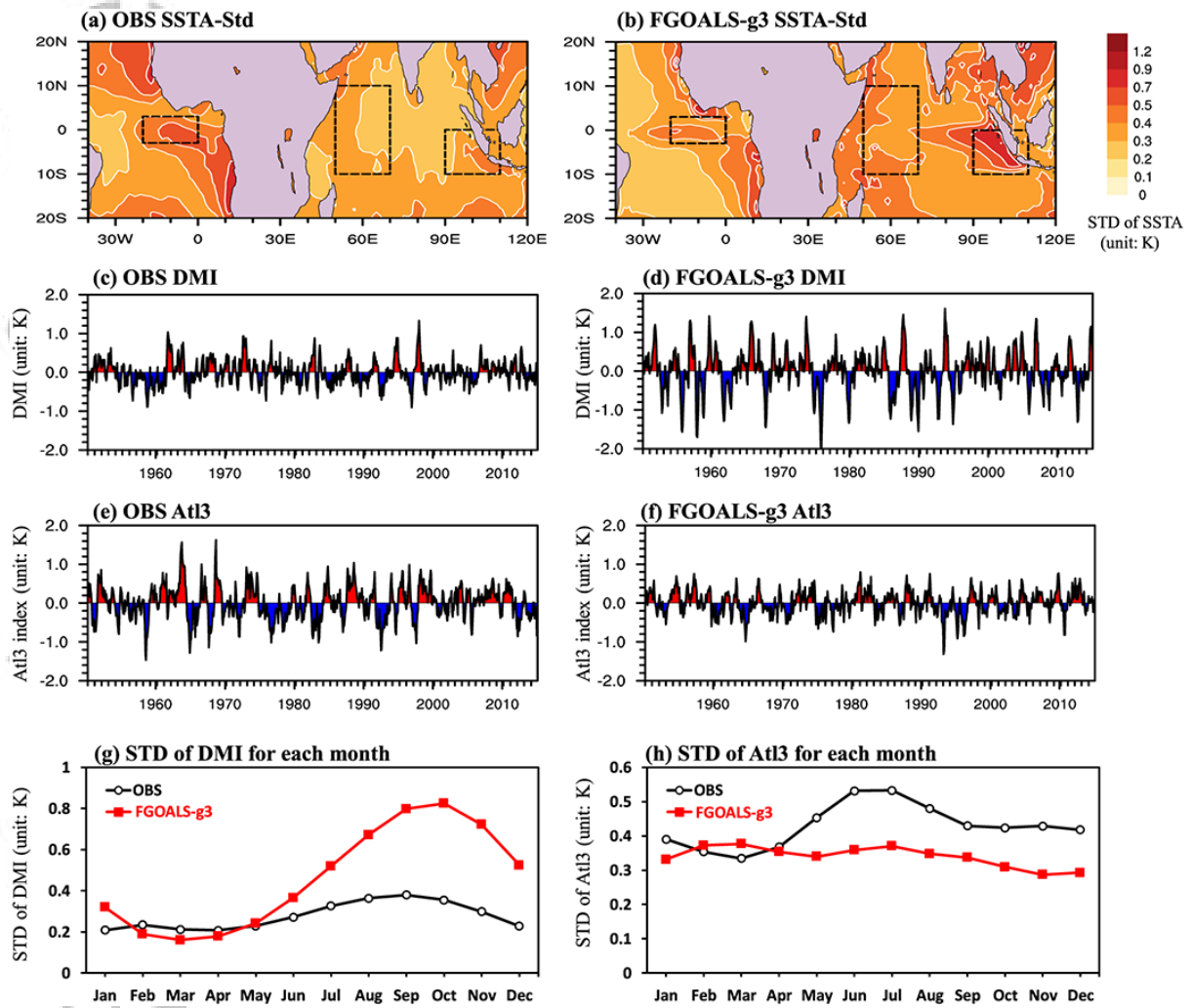


Figure 14. Spatial distribution of the standard deviation of the interannual anomaly of SST over tropical Atlantic and Indian Ocean, derived from (a) the observation and (b) the FGOALS-g3 historical simulation. The box in Atlantic denotes the Atlantic Niño3 region (20°W–0°, 3°N–3°S), and the two boxes in Indian Ocean denote the western pole of IOD (IODW; 50°E–70°E, 10°N–10°S) and eastern pole of IOD (IODE; 90°E–110°E, 0°–10°S). Time series of DMI (c–d) and Atlantic Niño3 index (e–f) for the observation and FGOALS-g3. Standard deviations of (g) DMI and (h) Atlantic Niño3 index for each calendar month. Unit is K for each panel.

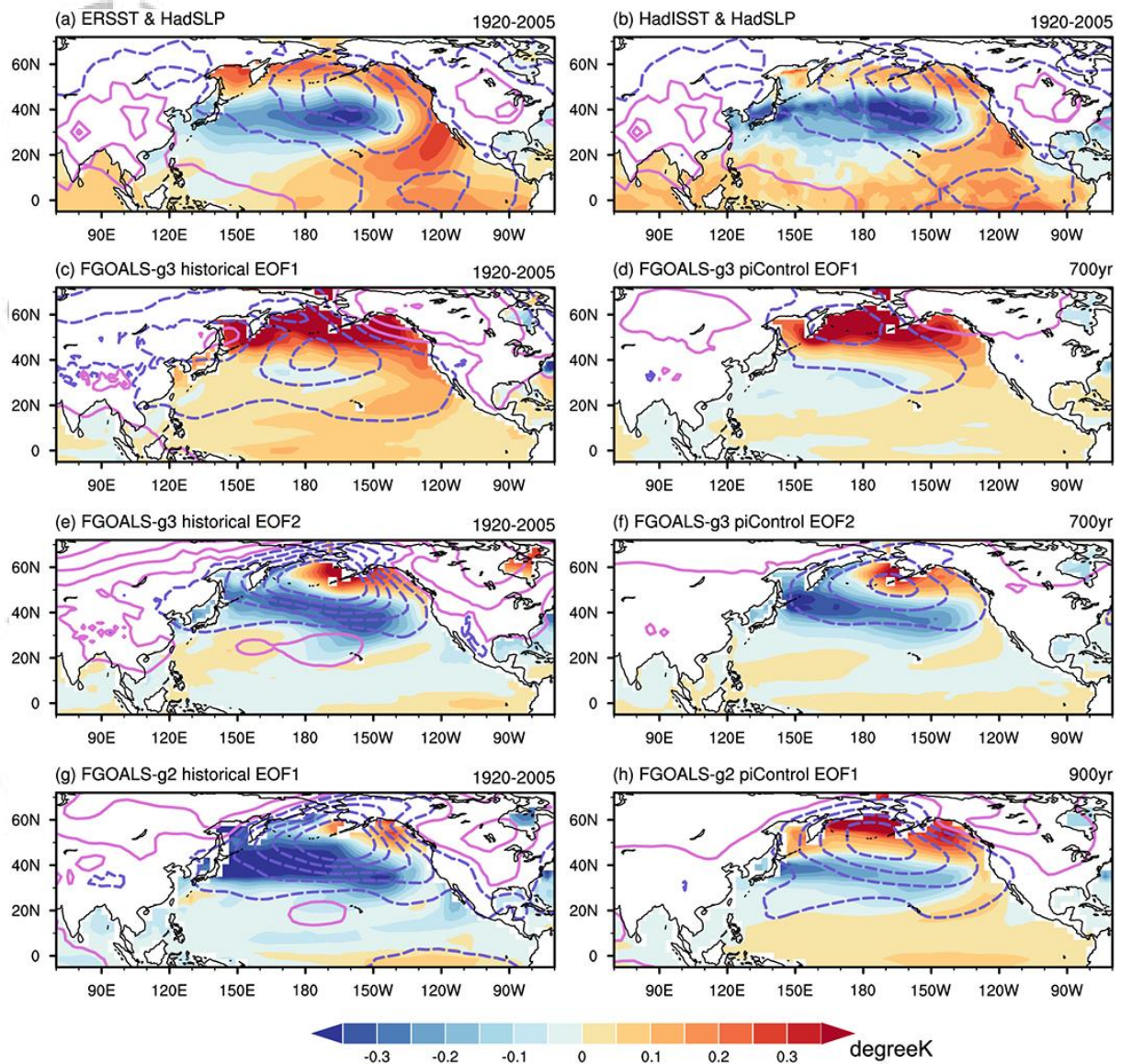


Figure 15. SST (shading, units: K) and SLP (contours, units: hPa) anomalies regressed onto the standardized PDO index during 1920-2005 from: (a) ERSST and (b) HadISST. SST (shading, units: K) and SLP (contours, units: hPa) anomalies from FGOALS-g3 historical run regressed onto (c) the PC1 and (e) the PC2 of the EOF analysis over the North Pacific. (d) and (f) are same as (c) and (e) but for the 700-year piControl run of FGOALS-g3. SST (shading, units: K) and SLP (contours, units: hPa) anomalies regressed onto the PC1 of the EOF analysis over the North Pacific from (g) the historical run and (h) the 900-year piControl run of FGOALS-g2.

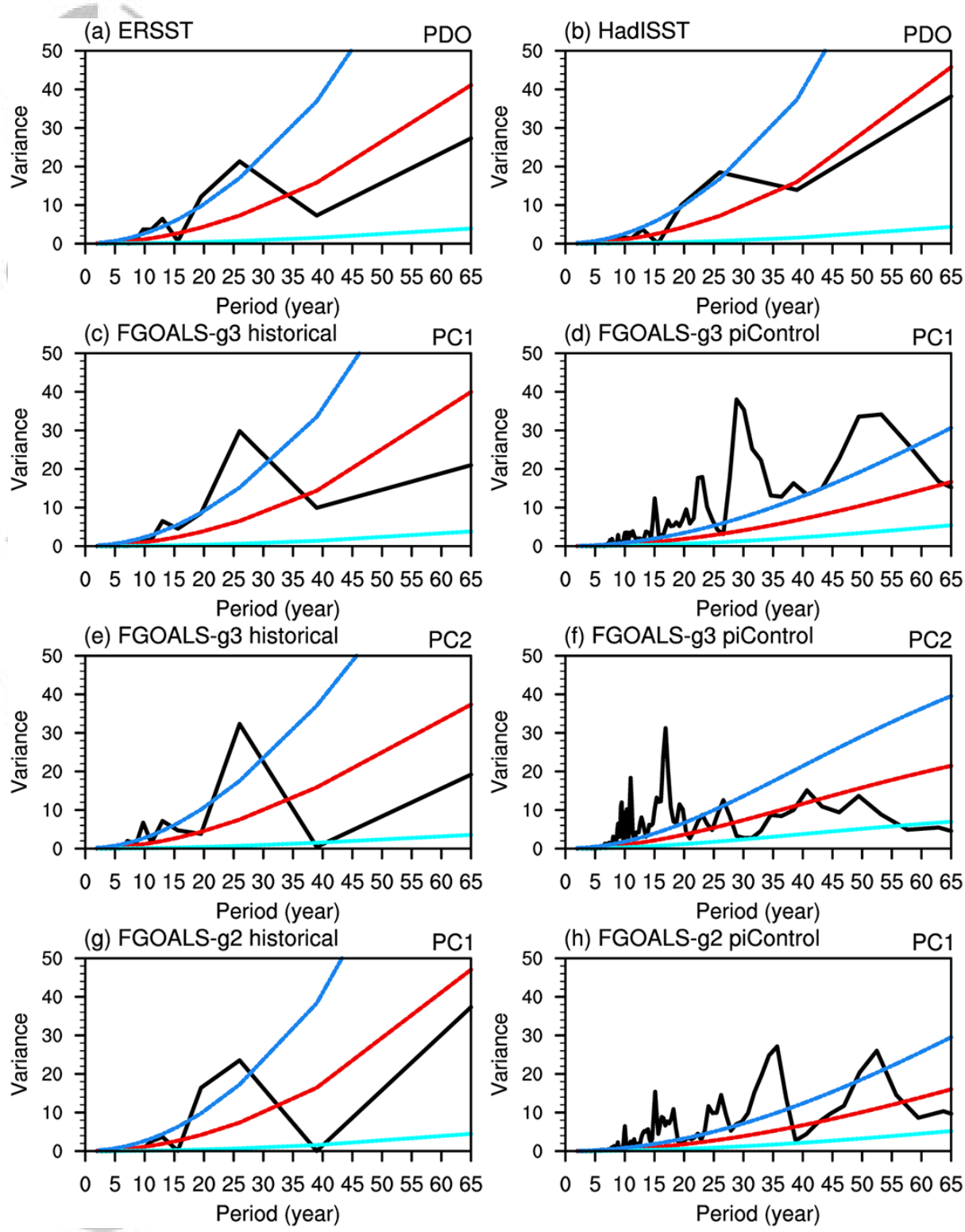
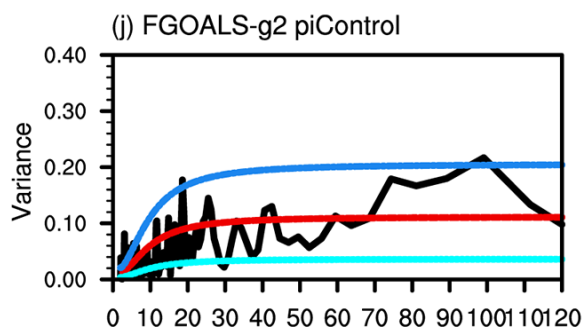
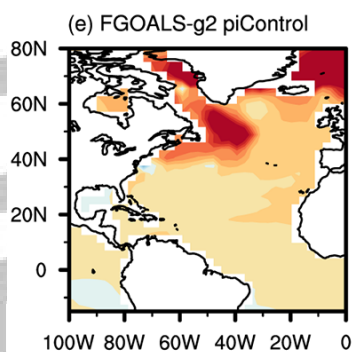
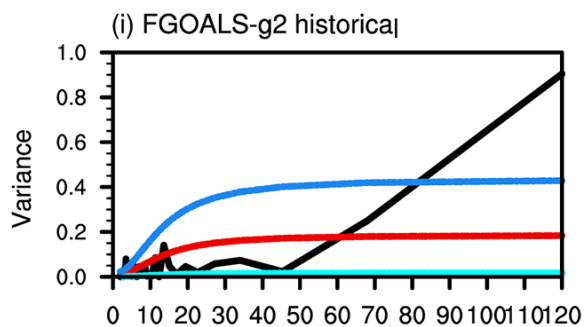
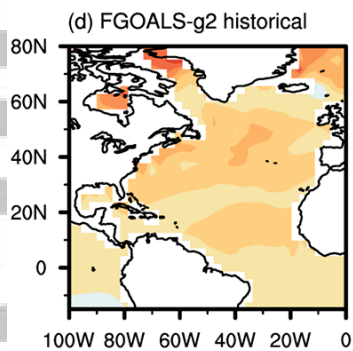
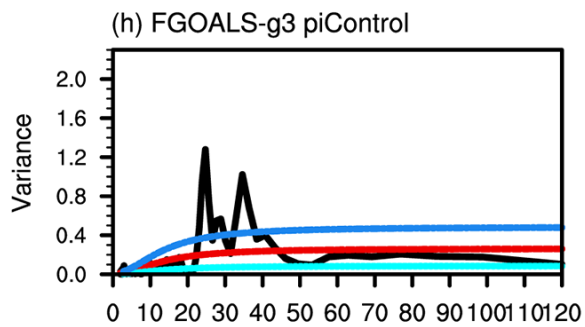
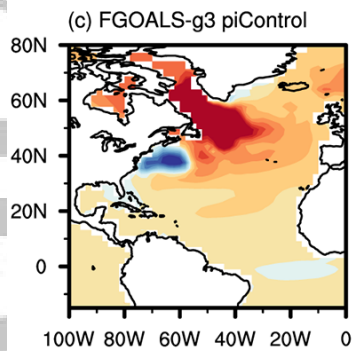
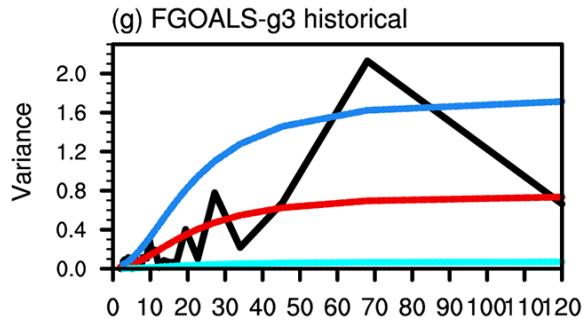
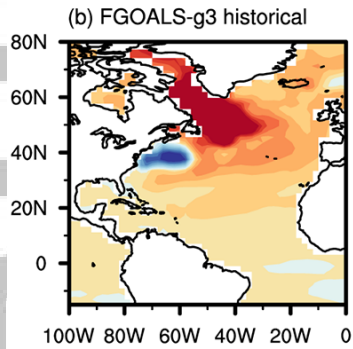
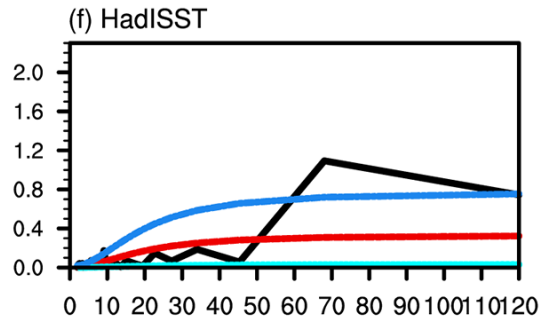
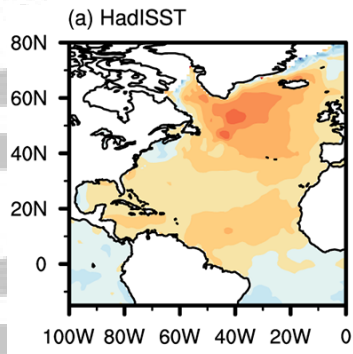


Figure 16. Power spectra (black lines) of: (a) the PDO index from the ERSST, (b) the PDO index from the HadISST, (c) the PC1 of FGOALS-g3 historical runs, (d) the PC1 of FGOALS-g3 piControl runs, (e) the PC2 of FGOALS-g3 historical runs, (f) the PC2 of FGOALS-g3 piControl runs, (g) the PC1 of FGOALS-g2 historical runs, (h) the PC1 of FGOALS-g2 piControl runs. The red, blue and light blue lines represent the power spectra of red noise, the 10% and 90% confidence level, respectively.



-0.48 -0.24 0 0.24 0.48 degreeK

Period (Year)

Figure 17. SST anomalies regressed onto the standardized AMO index: (a) HadISST, (b) FGOALS-g3 historical runs, and (c) FGOALS-g3 700-year piControl run, (d) FGOALS-g2 historical runs, (e) FGOALS-g2 900-year piControl run. Power spectra of the AMO indices (black lines) from: (f) the HadISST, (g) historical runs and (h) 700-year piControl run of FGOALS-g3, (i) historical run and (j) 900-year piControl run of FGOALS-g2. The red, blue and light blue lines represent the power spectra of red noise, the 10% and 90% confidence level, respectively.

Accepted Article

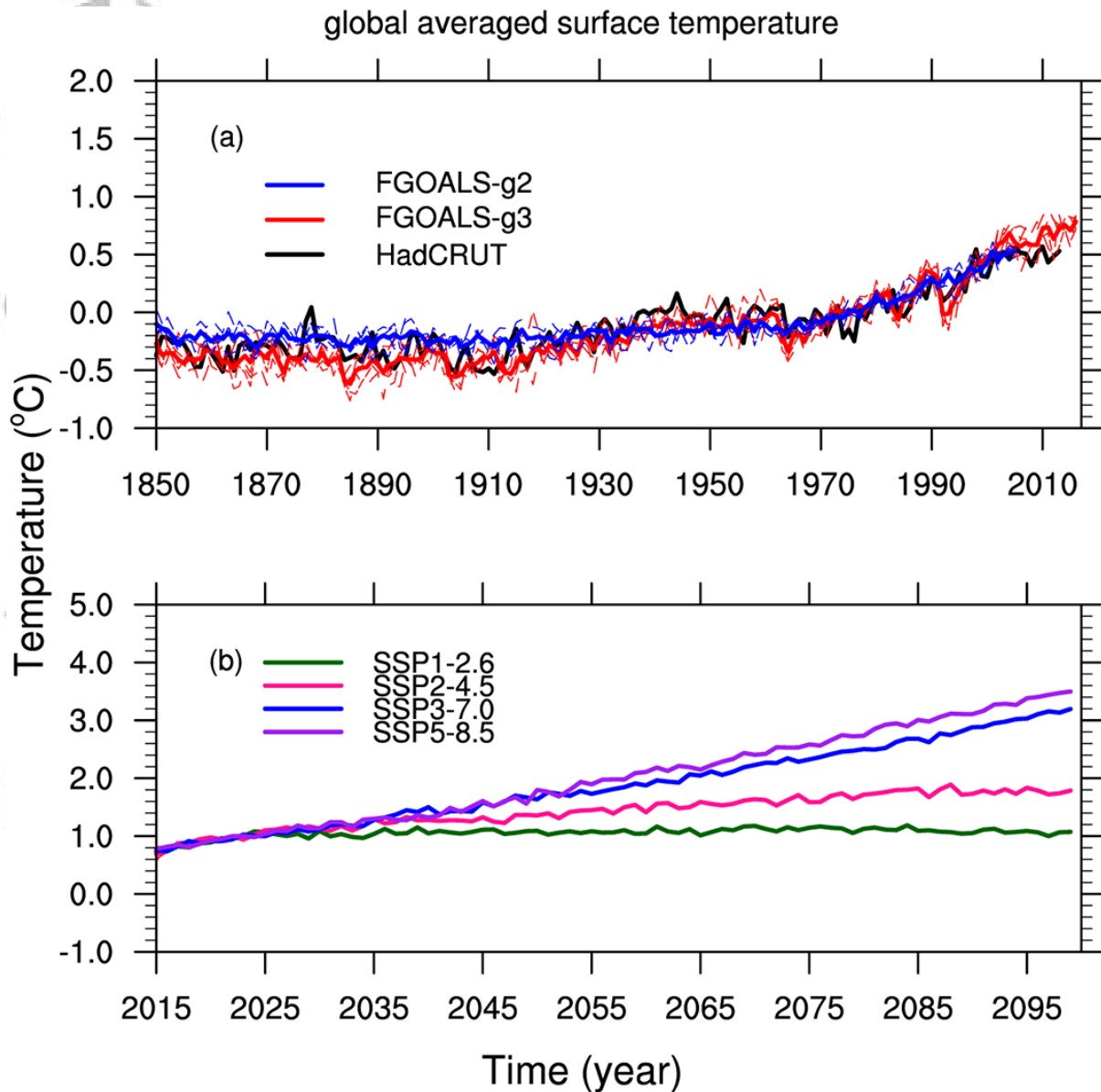


Figure 18. Time-series of the global surface temperature anomalies (°C) for (a) the historical runs by FGOALS-g3 (red lines; the thin red line is the different member run and the thick red line is the ensemble mean) and FGOALS-g2 (blue lines; the thin line is the different member run and the thick line is the ensemble mean), and (b) four future scenario runs by FGOALS-g3 (SSP1-2.6 = green line; SSP2-4.5 = pink line; SSP3-7.0 = blue line; SSP5-8.5 = purple line) relative to the period 1960–1990 (i.e., the 1960–1990 average is zero). For comparison, the observation during the historical period (black line) is also shown in (a).

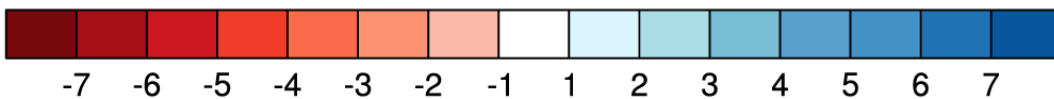
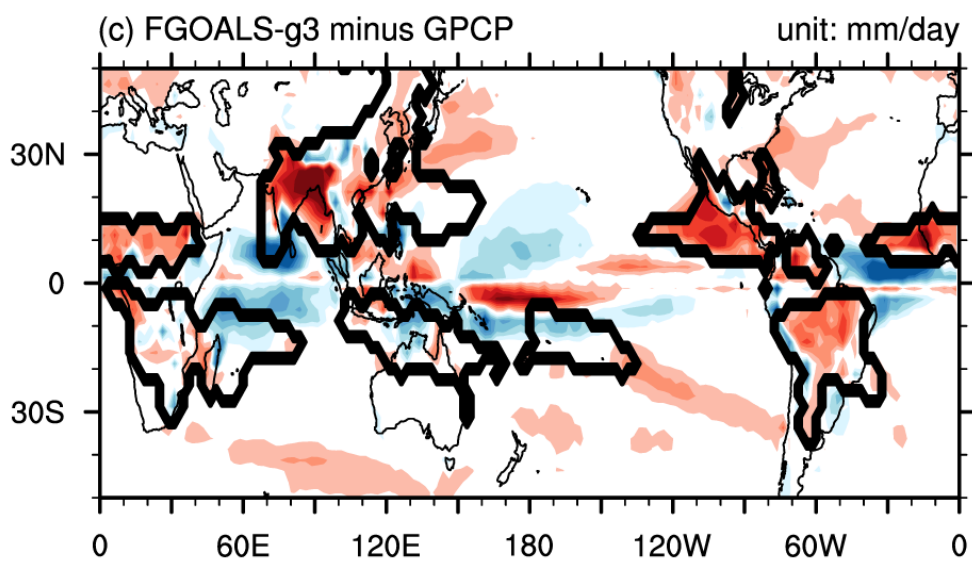
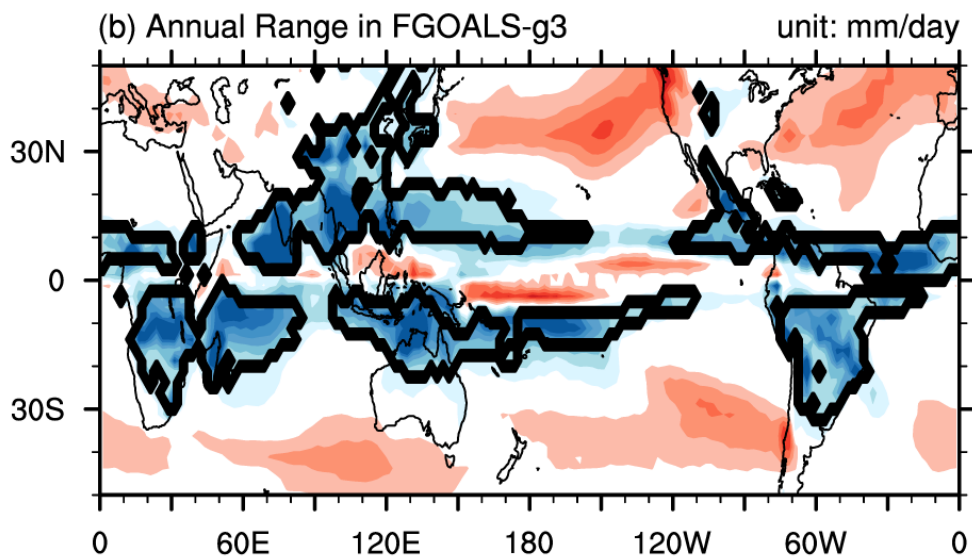
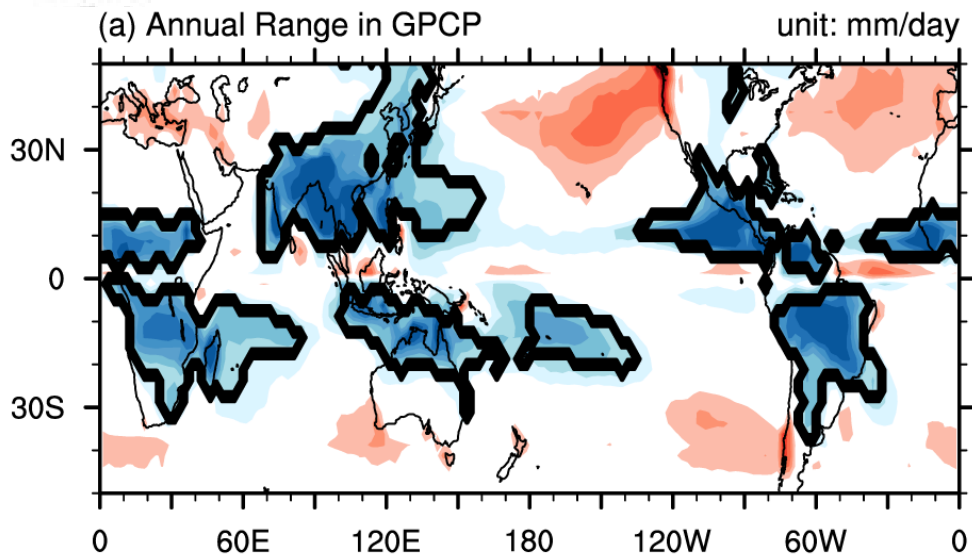


Figure 19. The climate mean global monsoon domain (black contours) and annual range of precipitation (shading, mm/day) for (a) GPCP and (b) FGOALS-g3. (c) is same as (a), but for the difference between FGOALS-g3 and GPCP and the monsoon domain is from GPCP. The annual range is the local summer-minus-winter precipitation. The monsoon domain is the region where annual range exceeds 2 mm/day and the local summer precipitation exceeds 55% of the annual total (Wang & Ding, 2008).

Accepted Article

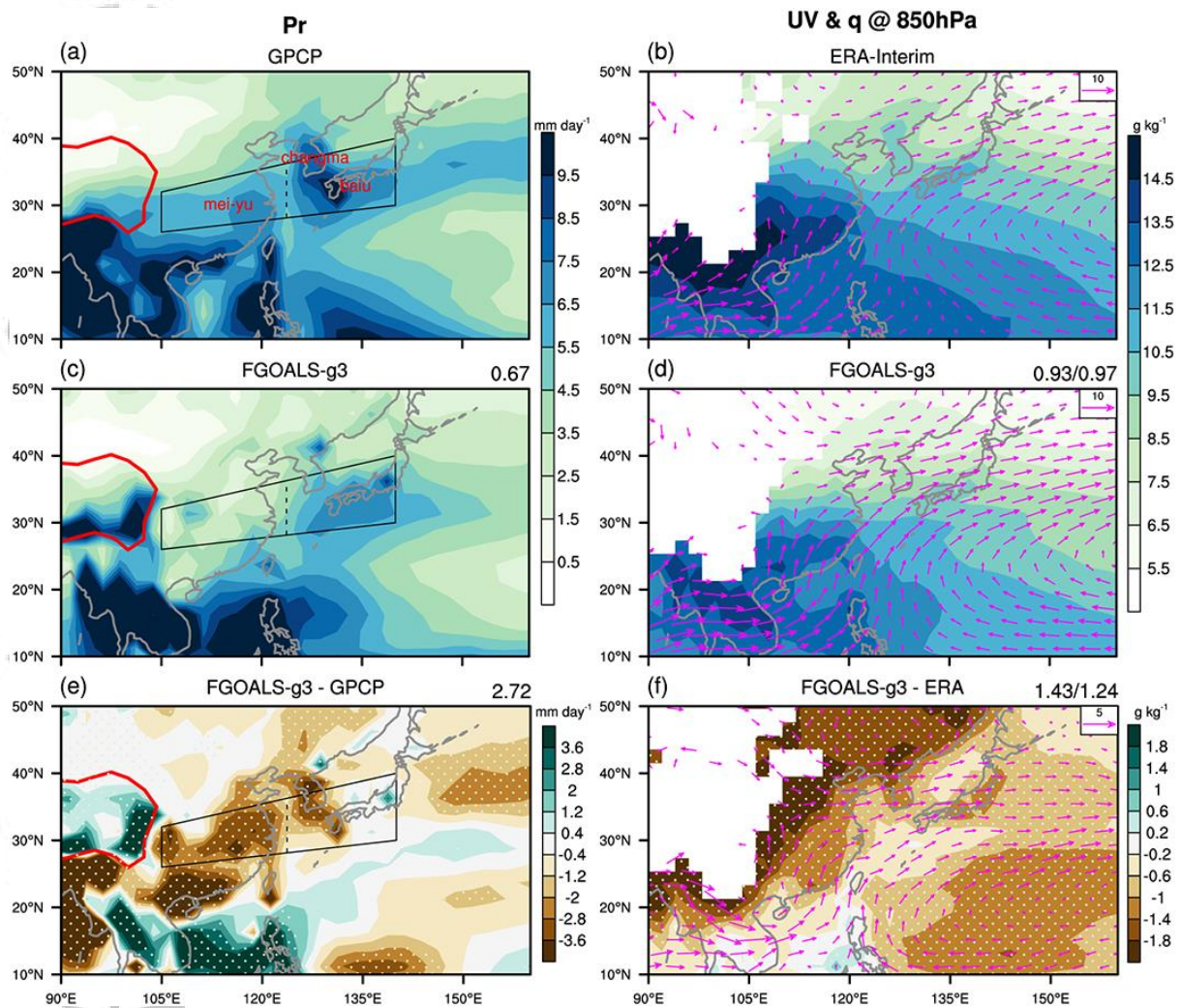


Figure 20. JJA mean (left column) precipitation (shadings; mm day^{-1}), (right column) horizontal wind (arrows; m s^{-1}) and specific humidity (shadings; g kg^{-1}) at 850 hPa. (a) and (b) are observational results from GPCP and ERA-Interim, respectively. (c) and (d) are FGOALS-g3 results. (e) and (f) are the biases between FGOALS-g3 and the observations. Red contours in (a), (c) and (e) denote topography above 2500 m. Values on the top-right in (c) and (d) are pattern correlation coefficients, and in (e) and (f) are root-mean-square errors. The black boxes in (a), (c) and (e) denote the mei-yu/baiu/changma region. Dotted shadings in (e) and (f) denote biases exceeding 1% significance level.

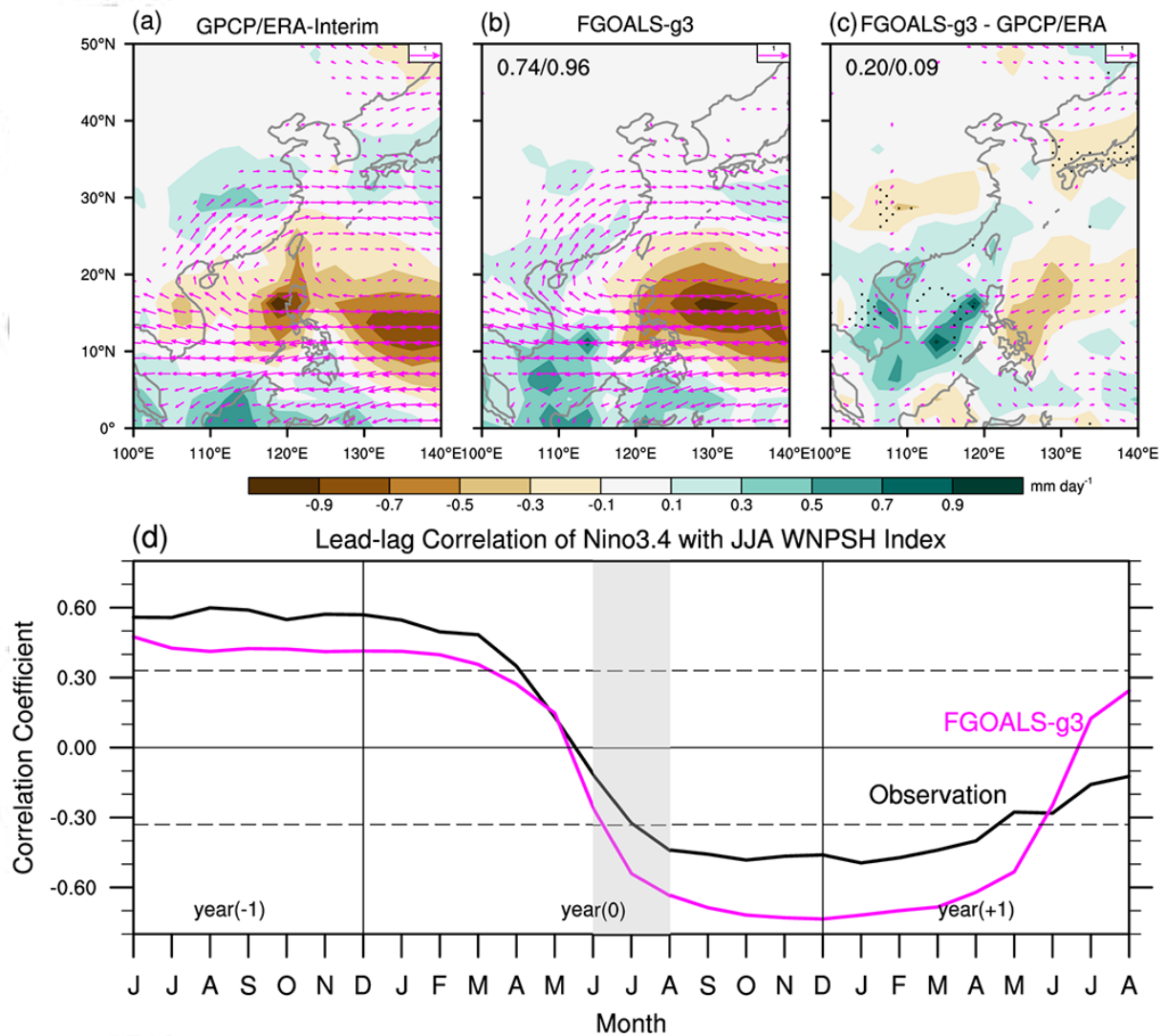


Figure 21. JJA precipitation (shadings; mm day^{-1}) and 850 hPa wind (arrows; m s^{-1}) anomalies regressed onto the WNPSH index (zonal wind difference between 22–32°N, 110–140°E and 5–15°N, 100–130°E) from (a) GPCP and ERA-Interim and (b) FGOALS-g3, and (c) the difference between (a) and (b). Dotted shadings in (c) denote biases exceeding 5% significance level. (d) Lead-lag correlation coefficients between the Niño3.4 index (sea surface temperature in 5°S–5°N, 170–120°W). Dashed lines denote 5% significance levels based on t-test. Values in (b) and (c) are pattern correlation coefficients and root-mean-square errors, respectively, for the precipitation and wind anomalies.